OS

REMOTE SENSING OF OCEAN CURRENTS WITH ERTS-1

George A. Maul
National Oceanic and Atmospheric Administration
Atlantic Oceanographic and Meteorological Laboratories
15 Rickenbacker Causeway
Miami, Florida 33149

August 1974
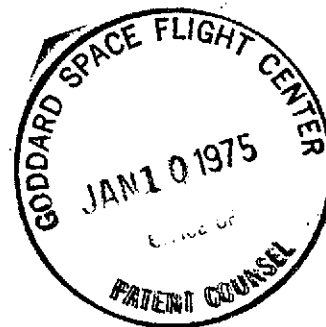Final Report for Period May 1972 - August 1974

Prepared for
GODDARD SPACE FLIGHT CENTER
Greenbelt, Maryland 20771

1108 A

TRIP TIC
Accession number
E75-10229

	Pub	Rec'd	Action	MF print
	7514	0000	BAMA	M

# Pages	Order Stk	Print	PC Due	Add'l Info y=See Bin List
0085	n	n	n	n

1. Report No.	2. Government Accession No.	3. Recipient's Catalog No.
4. Title and Subtitle REMOTE SENSING OF OCEAN CURRENTS WITH ERTS-1		5. Report Date August 1974
		6. Performing Organization Code
7. Author(s) George A. Maul		8. Performing Organization Report No.
9. Performing Organization Name and Address NOAA/AOML 15 Rickenbacker Causeway Miami, Florida 33149		10. Work Unit No.
		11. Contract or Grant No. GSFC ID C0315
		13. Type of Report and Period Covered
12. Sponsoring Agency Name and Address		Final Report May 1972 - August 1974
		14. Sponsoring Agency Code
15. Supplementary Notes		

16. Abstract ERTS data have been used to locate ocean currents in the Gulf of Mexico where summer surface temperatures prohibit the use of infrared techniques. The Gulf Loop Current was located by ship on a 36-day schedule in synchronization with the satellite. These studies have shown the current to have an annual cycle of penetration and recession that dominates the eastern Gulf. ERTS has been useful in proving that under the proper conditions, an ocean color sensing satellite can locate these baroclinic flows even in the subtropics, either by color changes, particle concentration changes or sea state changes. The edge of these currents are seen to be accumulation zones which show up as lineations on visible region sensors. It is shown from theoretical considerations that ERTS may be useful in detecting suspended particle concentrations if the ratio of the gradient of radiances in MSS 4 and MSS 5 is constant. This is shown to be realistic in regions where variations in Gelbstoff and chlorophyll are absent but is not always applicable in the coastal zone. Computer enhancement techniques are required to optimize information because the radiance level from ERTS over the ocean is low compared to the land. Spatially filtered, contrast stretched images provide the best radiance information for coastal zone monitoring and surface data analysis in the New York Bight.

17. Key Words (Selected by Author(s)) Detection of the color boundary layer.	18. Distribution Statement		
19. Security Classif. (of this report) Unclassified	20. Security Classif. (of this page) Unclassified	21. No. of Pages	22. Price*

*For sale by the Clearinghouse for Federal Scientific and Technical Information, Springfield, Virginia 22151.

Figure 2. Technical Report Standard Title Page

PREFACE

The objective of this investigation is to locate ocean current boundaries by sensing the color change associated with the cyclonic edge of the zone of maximum horizontal velocity shear. The test site is the eastern Gulf of Mexico where the strongly baroclinic flow from the Yucatan Straits forms into the Loop Current. The research is using ERTS' data in the investigation of ocean color sensing.

A time series of the location of the Loop Current was begun in August 1972. For every other transit of ERTS (i.e., 36 days) the current was located by ship. These data have been used to provide surface measurements in support of the spacecraft observations and to obtain the first time history of the circulation in the eastern Gulf of Mexico. These research cruises were conducted for over one year in order to understand the seasonal variability associated with the circulation and detection of the circulation's surface indicators.

Surface chlorophyll-a concentrations, which contribute to the shift in color from blue to green in the open sea, were found to have high spatial variability; significantly lower concentration were observed in the Gulf Loop Current. The cyclonic edge of the current is an accumulation zone which causes a peak in chlorophyll concentration. The dynamics of these currents also cause surface concentrations of algae, which have a high reflectance in the near infrared. Combining these observations gives rise to an "edge effect" which can show up as a bright lineation on multispectral imagery delimiting the current's boundary under certain environmental conditions. Frequently, the sea-state in the current is

higher than in surrounding water due to differential current shear. When high seas introduce bubbles, white caps, glitter, and foam, the reflectance is dominated by scattering rather than absorption. This has been detected in the imagery and used for current location.

The color effect relates to the spectral variations in the optical properties of the water and its suspended particles, and is studied by radiative transfer theory. Significant oceanic parameters identified are: the probability of forward scattering, and the ratio of scattering to total attenuation. Several spectra of upwelling diffuse light are computed as a function of the concentration of particles and Gelbstoff. These calculations compare favorably with experimental measurements and show that the ratio-of-channels method to determine ocean properties gives ambiguous interpretative results.

Subtle contrasts and low radiances observed by the ERTS multispectral scanner over the ocean require computer enhancement for adequate analysis. Experiments designed to evaluate contrast stretching, ratioing, differencing, smoothing, filtering, and false color enhancing, indicate that the best information can be extracted by simple contrast stretching. Spectral analysis of the data shows that a low pass, two-dimensional filter kernel, designed to be 3 db down at 10 scanspots, effectively eliminates the six-line banding caused by the multispectral scanner design. Automatic contouring techniques require careful scrutiny because data fields are created which can lead to false interpretations. Joint histograms of oceanic radiances did not prove to be useful due to the low range of energy in the several spectral intervals. Comparisons

of satellite data with surface ship observations confirm theoretical

predictions of the difficulty in interpreting scenes of the coastal zone.

TABLE OF CONTENTS

LIST OF ILLUSTRATIONS

HISTORICAL INTRODUCTION

Early work in the Gulf of Mexico has been summarized by Galtsoff
(1954) who edited a complete overview of the biology, chemistry, geology,
and physics of the area. In 1895, Lindenkohl published a map of the
temperature field at 250 fathoms (457 meters), in degrees farenheit,
which is reproduced in figure 1. The warm waters of the Caribbean can
be seen flowing northward into the Gulf and penetrating deeply into the
ambient thermal field; similarly the Gulf Stream, seen as a region of
large horizontal temperature gradient, is flowing easterly and then
northerly through the Strait of Florida. In an analysis of these data
Sweitzer, in 1898, reported that the circulation was a spreading of this
inflow which resulted in an anticyclonic circulation around the entire
Gulf basin. Parr, in 1935, reported the opposite conclusion using
ATLANTIS data taken in 1933: the Gulf Stream takes only the shortest
path from Yucatan to the Strait of Florida. Even after reviewing
Dietrich's 1939 map of the salinity maximum core, which reflects the
deep penetration seen in figure 1, Leipper expressed this divergence of
opinion as the state of knowledge in 1954. Work done in the 1960's,
notably by Leipper, Cochrane, Nowlin, and others at Texas A&M University,
led Leipper (1970) to speculate that there was an annual cycle in the
current patterns in the eastern Gulf. A time-series to establish the
seasonality was reported by Maul (1974). This paper is a preliminary
descriptive report on the time history of the current from August 1972
to September 1973.
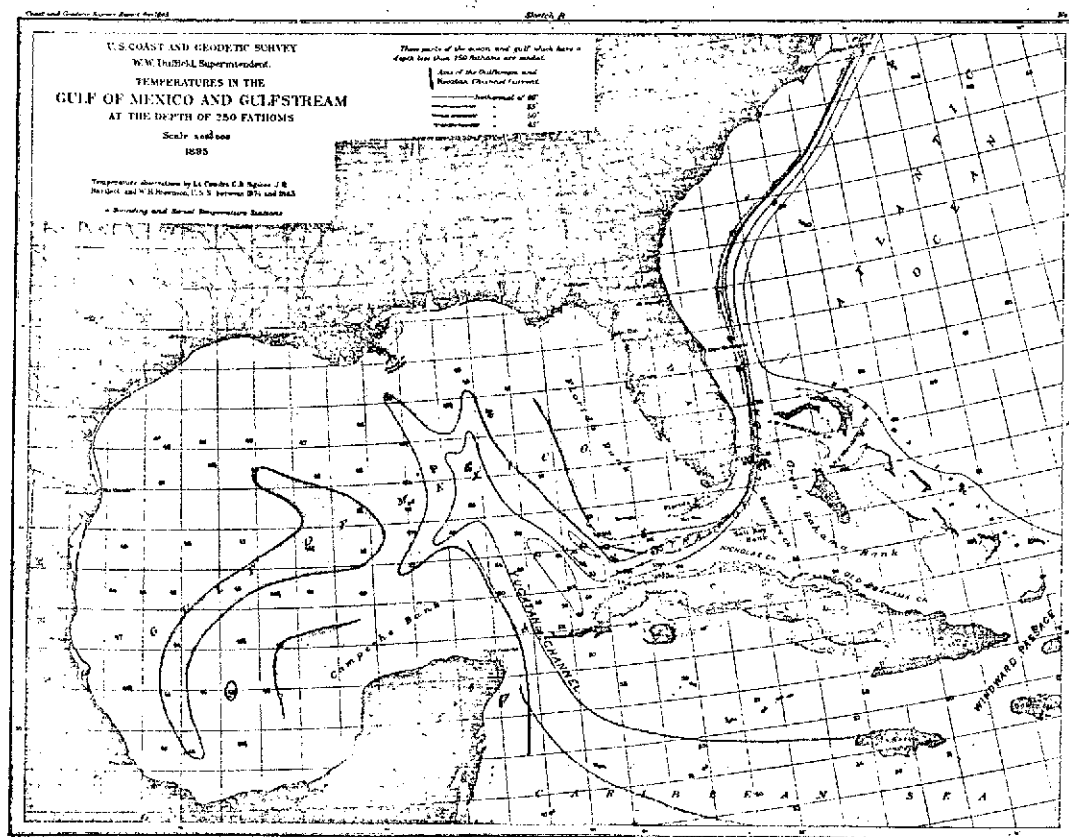
Figure 1. Lindenkohl's 1895 map of the temperature field (°F) at 250 fathoms in the Gulf of Mexico. Data are from soundings made by Sigsbee, Bartlett, and Brownson between 1874 and 1883. The shallow waters (<250 fms) of Campeche Bank and the west Florida Shelf, strippled on the chart, outline the topographic constraints of the Gulf Loop Current.

OBSERVATION PROGRAM

The field work began in June 1972 with a ship/aircraft experiment designed to detect the color boundary of the Loop Current front south of Dry Tortugas. The NASA C-130 flew over the research vessel track which was oriented in the same azimuth as ERTS suborbital track. Seven altitudes were flown, at 100 mb decrements, over the ship. Aircraft data collection included RC-8 color and color IR photography as well as multispectral photography to simulate the ERTS MSS imagery, PRT-5 sea surface temperature profiles, Bendix 24 channel scanner data, and inflight recordings of atmospheric temperature, pressure and moisture.

Prior to the aircraft overflights the scientific crew aboard ship located the boundary. Measurements of ocean temperature, chlorophyll-a, volume scattering function, and salinity were made every ten meters down to 50 meters; Forel color, and upwelling and downwelling spectral irradiance were taken at each of the five stations that bracketed the front. During the overflights on the following day, closely spaced surface measurements of the same variables (except irradiance) were taken. All measurements were made using standard oceanographic techniques or analyzed by methods detailed by Strickland and Parsons (1968).

The sequence of pathlines of the Gulf Loop Current was started to obtain the location of the cyclonic edge by ship in order to evaluate several methods of location by satellite. Figure 2 is a cross-stream transect taken on May 1, 1973, from north to south along the suborbital track of the Earth Resources Technology Satellite (ERTS). Speed of the vessel was about 10 knots, so the horizontal distance traveled from 1200

- 3 -
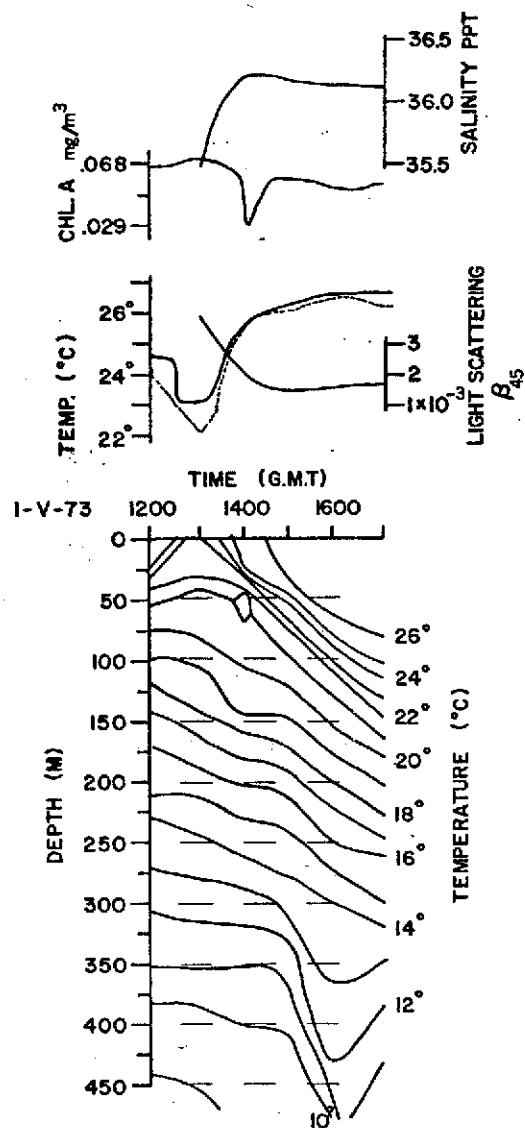
Figure 2. Thermal cross-section of the Gulf Loop Current on 1 May 1973 northwest of Dry Tortugas. Horizontal distance for the five-hour run is 90 kilometers. Bucket temperature (hourly) is solid line and radiometric (10.5 - 12.5 µm) temperature is dashed; other variables connect to their respective ordinate. The indicator isotherm is 22°C at 100 meters, which is approximately 20 kilometers to the right of the maximum surface thermal gradient facing downstream.

to 1700 GMT is approximately 90 kilometers.

Cross-section plots of surface salinity (hourly), chlorophyll-a (continuous; Lorenzen, 1966), volume scattering function, B_{45} (hourly), radiometric surface temperature (dashed; continuous), and bucket temperature (solid; hourly) are drawn above the cross-section of temperature down to 450 meters. Figure 2 is oriented such that the current flow is into the plane of the page and on the right-hand side (i.e., facing downstream). Surface observations are typical in that there is an increase of temperature and salinity, and a decrease of chlorophyll-a and scattering when entering the current from the cyclonic (left-hand edge facing downstream) side. The temperature field dominates the salinity to produce less dense water to the right in agreement with a geostrophically balanced flow; chlorophyll-a and scattering interact to cause a color shift from greenish-blue outside the current, to the cobalt blue so characteristic of this relatively sterile water mass.

Using the historical precedent of Leipper (1970) and others, the 22°C isotherm at 100 meters depth was chosen as an indicator of the current. This isotherm is approximately 20 kilometers to the right of the cyclonic edge, and near the surface velocity maximum. The observational strategy greatly improved tracking efficiency as it gave the research vessel an average boost of 2 knots. The actual tracking was done using expendable bathythermographs (XBTs). After observing hydrographic sections across the Florida Straits from Cosgrove Shoal to Havana, and across the Yucatan Straits from Cabo San Antonio to Isla Contoy, a zigzag tracking pattern was initiated. Typically, hourly BT's were taken.

- 5 -

When the depth of the 22°C isotherm exceeded 125 meters or so, the ship's course was altered 90° to the left. This course was run until the 22°C isotherm was less than 80 meters or so, and then course was altered to the right. The pattern was continued from Yucatan, around the Loop to Dry Tortugas, in all but a few cases, where weather or fuel considerations made it advisable to run for Key West. After each trip, the position data were replotted and a smooth plot constructed, which made a best fit to the estimated courses and speeds made good. Positioning was accomplished using Loran A, radar, visual, and celestial observations. It is difficult to estimate errors, but based on Loran A-radar comparisons, ± 1-3 kilometers seems reasonable.

The expendable BT data were adjusted so that the average surface reading on the strip chart recorder was in agreement with the average bucket temperature. The strip chart recorder was tested (and adjusted if necessary) before and after each cruise with a test canister. Infrared temperatures were calibrated using a blackbody source in the laboratory so that the radiometric temperatures could be compared to the bulk values. This latter comparison is necessary in order to study the infrared observations of the NOAA-2 scanning radiometer, and to properly interpret those data.

TIME SERIES OF THE CURRENT

Pathlines of the 22°C isotherm at 100 meters depth are summarized in figure 3. The series was obtained at 36-day intervals, coincidental with the 18-day period of ERTS. Dates of each survey are labeled on the
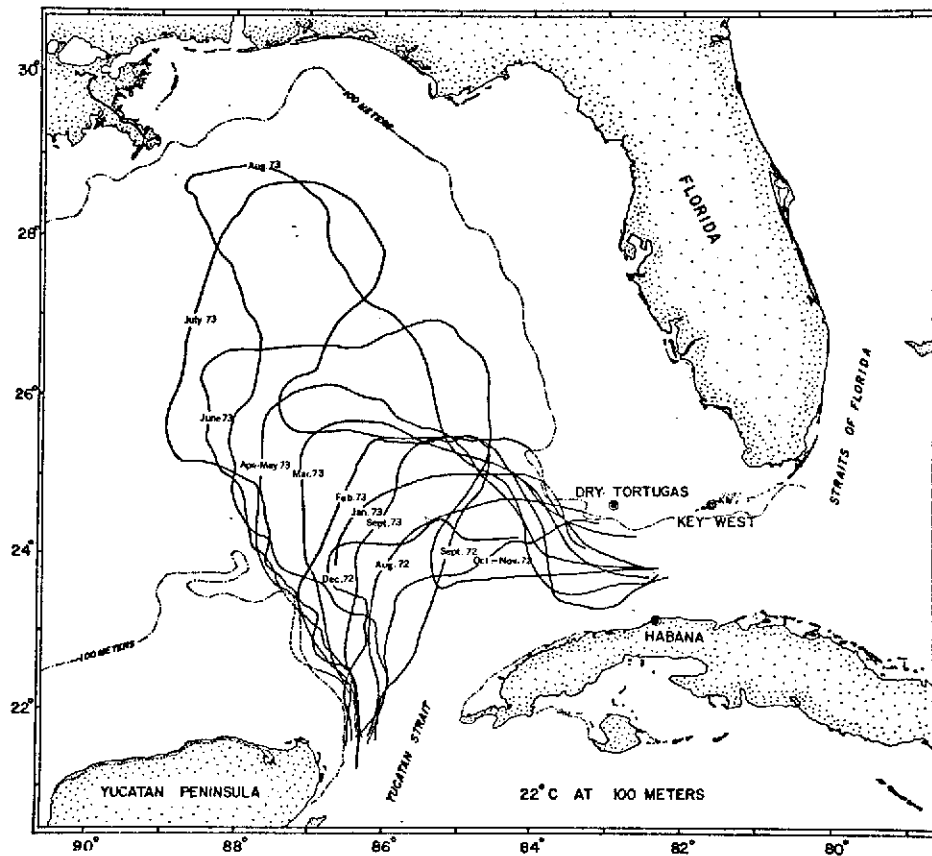
Figure 3. Pathlines of the 22°C isotherm at 100 meters from August 1972, through September 1973. Surveys were 36 days apart and in coincidence with every other transit of the Earth Resources Technology Satellite: where two months are given, the survey extended over the change of date. Cruises were from three to six days in duration and the research ship motored with a following current.

appropriate pathline; where the cruise started at Yucatan in one month and ended off Dry Tortugas in another, both months are labeled. The shortest tracking time was three days and the longest six days, so that near synopticity was accomplished. Hydrographic station transects of the straits added two days to each cruise. Conditions prior to the first cruise were that a large anticyclonic detached eddy was observed in May, 1972. The current flowed essentially north from the Yucatan Straits and curved in a gentle anticyclonic curvature, ending tangent to the Florida Keys platform.

By September conditions had changed markedly. The initial current direction had a significant easterly component and flowed directly toward the west Florida shelf. There was evidence of Loop Current water on the shelf, and the 22°C isotherm apparently went aground well north of Dry Tortugas. It is notable that a red tide of Gymnodinium breve was reported on the Florida shelf at this time. By late October the current had reformed to its southernmost extent, and evidence of Florida Bay water flowing south through the Keys was noted in both the ship track and an ERTS image. Murphy, et al. (1974) have used this evidence to partially document the source of the first reported Florida east coast red tide. Apparently the organisms were carried by the current through the Florida Straits and exchanged with local coastal water north of Miami.

By December 1972, the current had swung to the west and had penetrated into the Gulf to the same latitude as August. At 24°N, the stream flowed in a sharp anticyclonic turn to the east. January 1973 was the only month in which transects of the Straits were not obtained. This

- 8 -

was due to 50-knot winds and high seas forcing the ship to turn back.
Only four crossings were obtained but sufficient detail permitted
the observation, for the first time, that the current penetrated north
of Dry Tortugas (25°N).

The "spring intrusion" (Leipper, 1970) continued through February,
March, April-May, and June when the current extended to 27°N. As the
current penetrated deeper it also swung further to the west and seemed
to be controlled by the bottom topography of Campeche Bank in agreement
with a potential vorticity conserving flow as postulated by Molinari and
Cochrane (1972). North of 24°N the isobaths curve sharply to the west,
and the current flows into deeper water where different dynamics probably
dominate.

A deep intrusion in July 1973, coupled with a marked cyclonic curva-
ture off the west Florida shelf, led us to expect separation of an eddy
by the following cruise. The deep intrusion from the east was not a
sampling artifact; a second vessel from the State University System of
Florida Institute of Oceanography (SUSIO) obtained hydrographic station
data across the shelf and out into the main current throughout this area.
The furthest western extent of the current also occurred in July.

By August 1973, the current system extended almost to the Mississip-
pi Delta. The expected eddy had not separated. Very low salinity water
(<24°/oo) was recorded by the SUSIO vessel, again cooperating with the
NOAA ship, all along the current-edge off the Florida Shelf. The hydro-
graphic section in the Florida Straits had surface salinities less than
30°/oo along the cyclonic boundary. Since the Loop Current was so close

to the delta area, and there are no other significant sources of fresh water, it seems probable that this was Mississippi River water in origin.

During the last cruise, September 1973, the current was found well to the south again, at approximately the same penetration as February. A trackline from Ft. Myers, west to 87°W, and north to Pascagoula, confirmed that an anticyclonic eddy had indeed separated, and a significant change in the hydrography of the eastern Gulf had occurred in one month. There was no hint in the extensive August data that a recirculation had begun as a prelude to the eddy formation, although observations by Cochrane (personal communication, 1974) made between the April-May and June cruises, showed substantial closure in his isotherm field in this area.

Niiler and Richardson (1973) obtained a time series of the transport of the Florida Current between Miami and Bimini. These data, taken during 1964-1970, show a transport minimum in December and a maximum in June. The data in figure 3 show a minimum penetration into the Gulf in October-November and a maximum in July-August, which is in fair agreement with the average transport cycle.

EDGE EFFECT

The cyclonic edge of the Loop Current tends to concentrate flotsam and jetsam. Natural materials, such as surface marine algae, were seen from the June photography to have a pinkish cast on color IR (SO 397) film; this is confirmed in black and white IR photography (type 2424 film and a 89B Wratten Filter). When these algae are present, they appear

as a bright lineation marking the edge of the current in ERTS MSS-6
$(0.7-0.8\mu m)$.

A second consequence of the boundary layer dynamics is to concen-
trate chlorophyll bearing organisms. A typical profile across the cur-
rent boundary is given in figure 4. This transect is from Key West
harbor, out the channel into the coastal water, and across the front.
The feature of interest is the peak in chlorophyll-a concentration just
at the boundary. This is a phenomenon noticed frequently and occurs
to a varying degree in the deep sea as well as near shore. Details of
the variability will have to await further analysis (Ednoff, 1974) be-
cause of expected seasonal and biological dependence. One would expect
however that a shift towards the green would occur and enhance the boun-
dary in MSS-4$(0.5-0.6\mu m)$. This does indeed happen as will be discussed
below.

A third observation is the usual change in sea state across the
boundary. When winds and associated waves cross into zones of high cur-
rent velocity with an opposing set, the seas generally build up rapidly.
It is not uncommon for the sea state to increase from 1 to 2 meters when
crossing into the current. Thus an increase of white caps, foam, and
bubbles is encountered near the edge which increases the reflectance in
the current. This raises the reflectance in all channels, but in a non-
uniform (wavelength dependent) manner.

The term "edge effect" (Maul, 1972) was coined to describe these
phenomena which can be exploited to detect the boundary of major ocean
currents. Other streaming events, such as sediments being entrained by
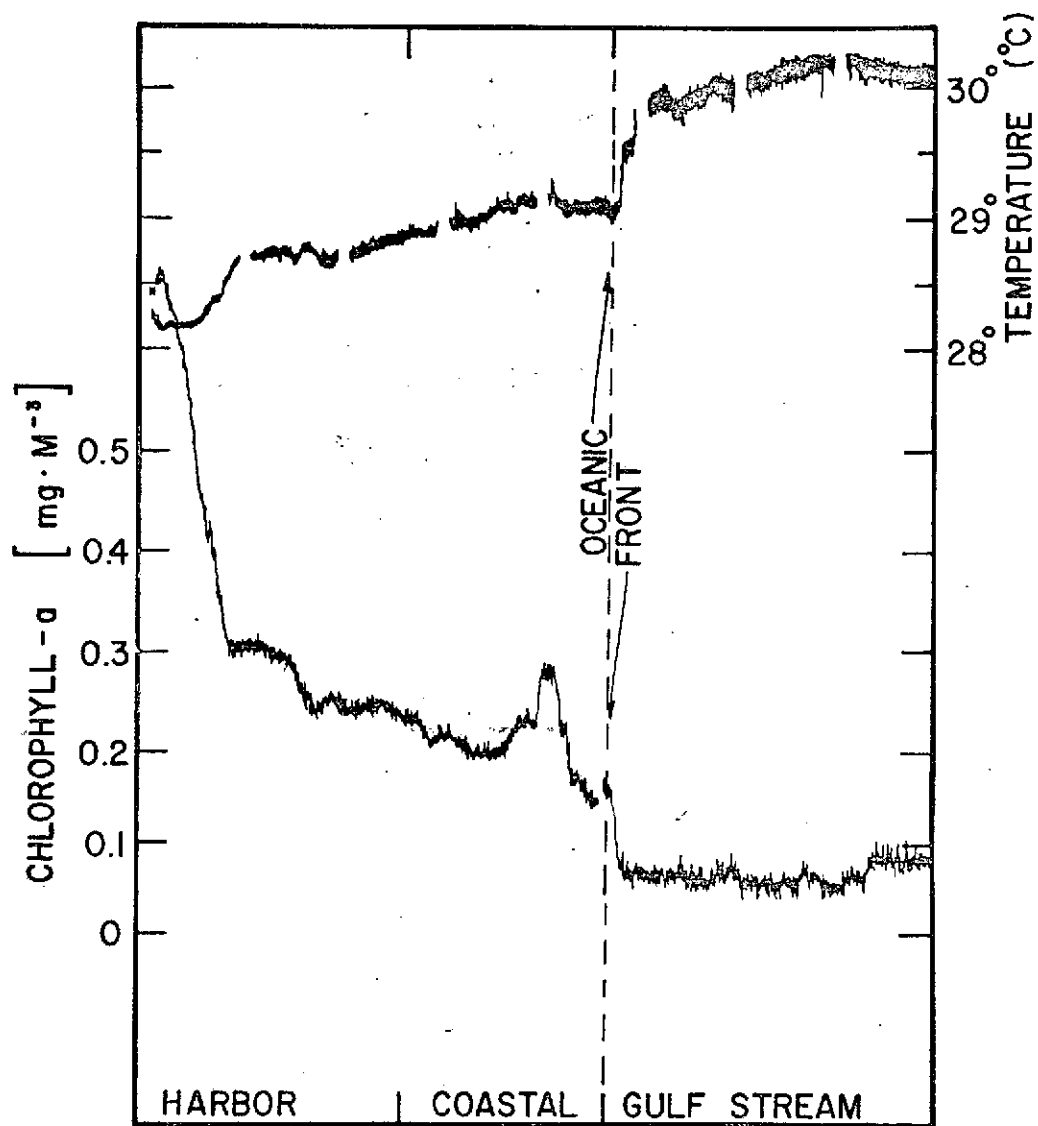
Figure 4. Surface temperature trace (upper) and surface chlorophyll-a profile (lower) across the Loop Current Front and into Key West Harbor. Horizontal scale across the figure is approximately 75 kilometers.

the Gulf Stream after passing source regions such as Cape Hatteras (c f. figure 13), can be considered part of this edge effect. It allows a multispectral approach to recognize the boundary of these currents in the absence of sea surface temperature changes.

ERTS OBSERVATIONS OF OCEANIC FRONTS

The location of the cyclonic boundary of the Loop Current was obtained by tracking the 22°C isotherm at 100 meters depth using expendable bathythermographs. The pathline of the isotherm is of the order of 20 kilometers to the right (facing downstream) of the surface frontal zone (Hansen and Maul, 1970). This, coupled with ship observations of chlorophyll-a, surface temperature, volume scattering function, and sea state, provides the baseline measurements to insure that the interpretations to follow are well founded. Figures 2 and 4 summarize the general conditions of increasing temperature and salinity and decreasing chlorophyll and scattering when crossing the boundary into the current and serve to orient them to the indicator isotherm. These observations confirm (Maul and Hansen, 1972) that changes in all these properties occur simultaneously, allowing an increase in confidence when a recognition decision is made using several variables.

Diffuse reflectance from beneath the ocean, which is defined as the ratio of upwelling to downwelling irradiance, measured just above the surface, is rarely more than 0.05. Reflectance from the ocean's surface, which is independent of diffuse reflectance, can be comparable or even substantially larger depending on sea state, and this has been shown by

Maul (1973) to be a useful indicator of the current. Reflectance from clouds and agricultural scenes is sometimes an order of magnitude greater than from the ocean, even in the 500-600 nm wavelength (λ) region. In order for the NASA Data Processing Facility (NDPF) to produce an image for an average scene radiance, the ocean signal is compressed into the lowest few gray scales. This is clearly illustrated in figure 5 which is a scanline plot across the boundary of the Loop Current from the multispectral scanner. The large spikes in all four channels (MSS 4 upper) are clouds; there seems at first glance to be very little change in digital number (DN), which is proportional to radiant intensity, as a function of the sample number. However, careful examination shows that the average value of the DN at samples greater than number 950 is slightly larger than those before this point. It will be seen that this marks the transition to higher radiances caused by increased sea state in the current.

CONTRAST STRETCHING

ERTS was not designed for ocean observations, however very early in the mission it became apparent that features of oceanographic significance were visible (e.g., Charnell and Maul, 1973). In the coastal zone, radiance changes as large as 0.23 mW cm^{-2}sr^{-1} may be encountered across the interface of a waste disposal site, but in the deep sea, changes of less than 0.016 mW cm^{-2}sr^{-1} occur across a current boundary. Ross (1973) was able to demonstrate a degree of success with optical enhancement techniques using ERTS images in coastal areas, but changes whose radiance differences are more than an order of magnitude less than those of waste
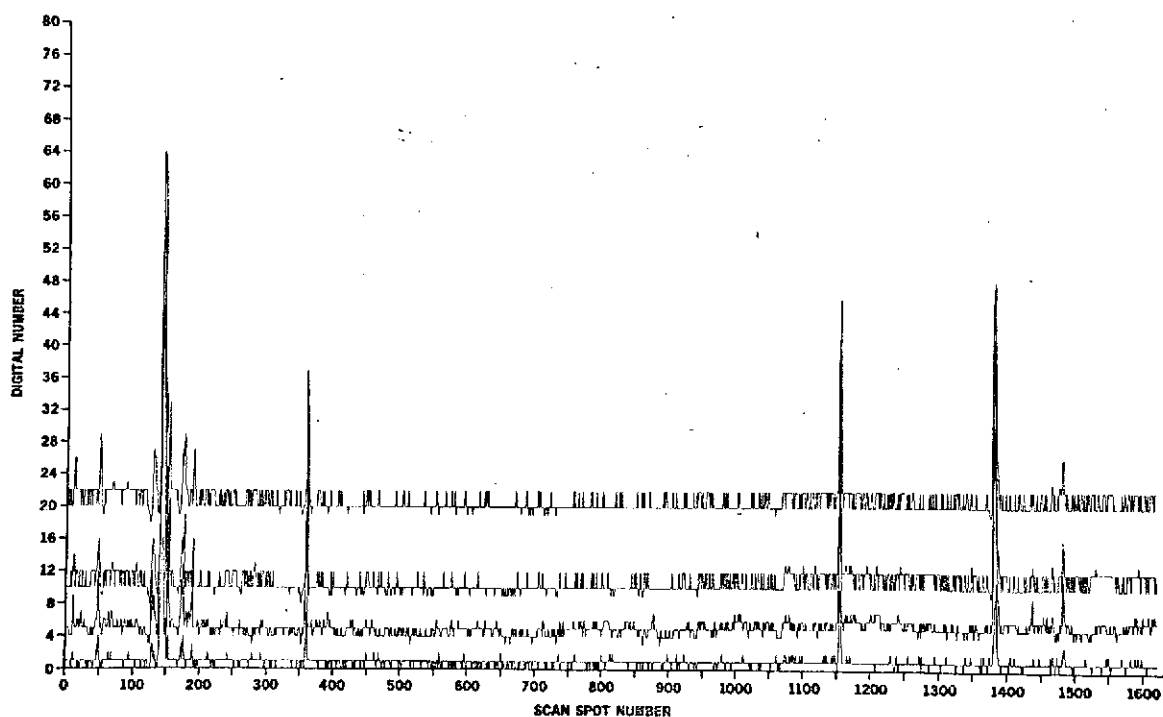
Figure 5. ERTS scanline plot across the Loop Current front. Top scanline is MSS 4, next MSS 5, MSS 6 and MSS 7 on the bottom. The large energy spikes are clouds. At scan spot number 950 there is an increase in the average value of the digital number of 1 or 2; this marks the cyclonic edge of the current.

- 15 -

dumps cannot be optically enhanced because their signature is insufficiently defined in the original film product. Any signatures sensed at all, however, will be in the digital data because ERTS digitizes the multispectral scanner (MSS) output onboard the spacecraft; such data are therefore first generation information. Further, using the digital product permits actual radiances to be manipulated, thus avoiding certain vagaries associated with films, chemicals, and optical transforms.

The full range of 128 digital number (DN) steps on MSS 4 (0.5-0.6 μm) MSS 5 (0.6-0.7 μm), and MSS 6 (0.7-0.8 μm), and 64 steps on MSS 7 (0.8-1.1 μm) are required in order to digitize the range of radiances observed from the earth in each of these bandpass intervals. Figure 5 summarizes the range of DN in the open ocean; other scanline plots show that DNs averaging 50 ($\sim$0.97 mW cm^{-2}sr^{-1}) are typical over the land in MSS 4, but oceanic values in this channel average 20 ($\sim$0.39 mW cm^{-2}sr^{-1}). In addition, the range of DNs over the land is much greater (ΔDN$\sim$25) as compared to the water (ΔDN$\sim$8).

For the ocean scene then, all the information is constrained to a low level, and to a low range, of radiance. In order to optimize a display of this information, a narrow range of DNs expanded about the mid-value of the ocean DN levels must be used. To do this a sub-matrix of pixels (called the training area), approximately 500 x 500 elements, of "cloud-free" ocean radiances are analyzed statistically for their mean ($\overline{DN}$), standard deviation (σ), and frequency distribution. If the training area is carefully chosen to be representative of the range of oceanic radiances, and the distribution is Gaussian, then 95% of all data are included in the range $\overline{DN} \pm 2\sigma$.

To insure inclusion of all values in the original data, with emphasis on a certain range, a mapping algorithm for the stretch variable ($\bar{\zeta}$) must be chosen. If M is defined as the maximum value that the D/A converter can accept as an input voltage, a simple expression for contrast stretching is:

$$\zeta = \frac{M}{2}\left[1 + \tanh\left(\frac{DN-\overline{DN}}{n\sigma}\right)\right]$$

where n is a constant. The distinct advantage of a continuous function such as a hyperbolic tangent is that all values are included and their weights are adjusted according to the value of n. Several disadvantages such as nonlinearity of output and computational inefficiency favor a stretch variable of the form

$$\left.\begin{aligned} \zeta &= M, \text{ for } DN \leq \overline{DN} - 2\sigma \\ \zeta &= M\left[\frac{(\overline{DN} + 2\sigma) - DN}{4\sigma}\right]^{n}, \text{ for } -2\sigma < (DN - \overline{DN}) < +2\sigma \\ \zeta &= 0, \text{ for } DN \geq \overline{DN} + 2\sigma. \end{aligned}\right\} \quad (1)$$

Equation 1 thus produces a negative, linear (for n = 1), statistically based contrast stretched image, of the data in the interval $\overline{DN} \pm 2\sigma$. A positive image could be produced if the numerator of the bracketed term in (2) were changed to $DN - (\overline{DN} - 2\sigma)$, and the limits on $\zeta = 0$ and $\zeta = M$ were reversed.

Since ocean features are always at the low end of the radiance range, it is sometimes advantageous to be able to emphasize them by a non-linear stretch. Equation 1 will allow this by setting n = 2, 3, etc. If the positive version of equation 1 is used, then n = 1/2, 1/3, etc. for

- 17 -

stretching the low DN values (at a great cost in computational efficiency). If a cloud-free training area is analyzed for its statistics, this objective mapping algorithm allows a one-step computational effort. Using $n = 1$ is generally preferred since it produces a grayscale that is linear in radiance. In every case, the histogram from the training area's statistics should be studied to insure that the frequency distribution has a Gaussian form. If land or clouds were inadvertently included in the training area, or the area is too small, a non-Gaussian form will be encountered.

Figure 6 is a negative print of an area due north of the Yucatan Straits using MSS 5 data; the scanline from figure 5 was taken through the center of this image. Computer enhancement in this image uses only five gray scales of the 128 levels available; all values below $\zeta = M$ are set to 0. The boundary between the resident Gulf waters (left) and the current (right) is seen as a transition from light to dark tones respectively. Since the radiance levels in the ocean are so low, the oceanographer must resort to computer enhancement as this example shows.

Figure 7 is another enhancement of the Loop Current boundary using MSS 5 where $7 \le DN \le 15$ and $n = 2$. In this negative image of the western Florida Keys, water from Florida Bay extends into the Florida Straits and is entrained by the Loop Current. The current boundary in both figures 4 and 5 was delineated by surface vessel tracks during the day of the satellite transit. Notice that the current is darker in tone (higher in radiance) in figure 5. This is caused by the dominance of surface reflection due to higher sea state in the current in figure 5, as compared to higher reflectance due to particles in the Florida Bay water in figure 7.

FLORIDA BAY

KEY WEST

FLORIDA CURRENT FRONT

CLOUDS
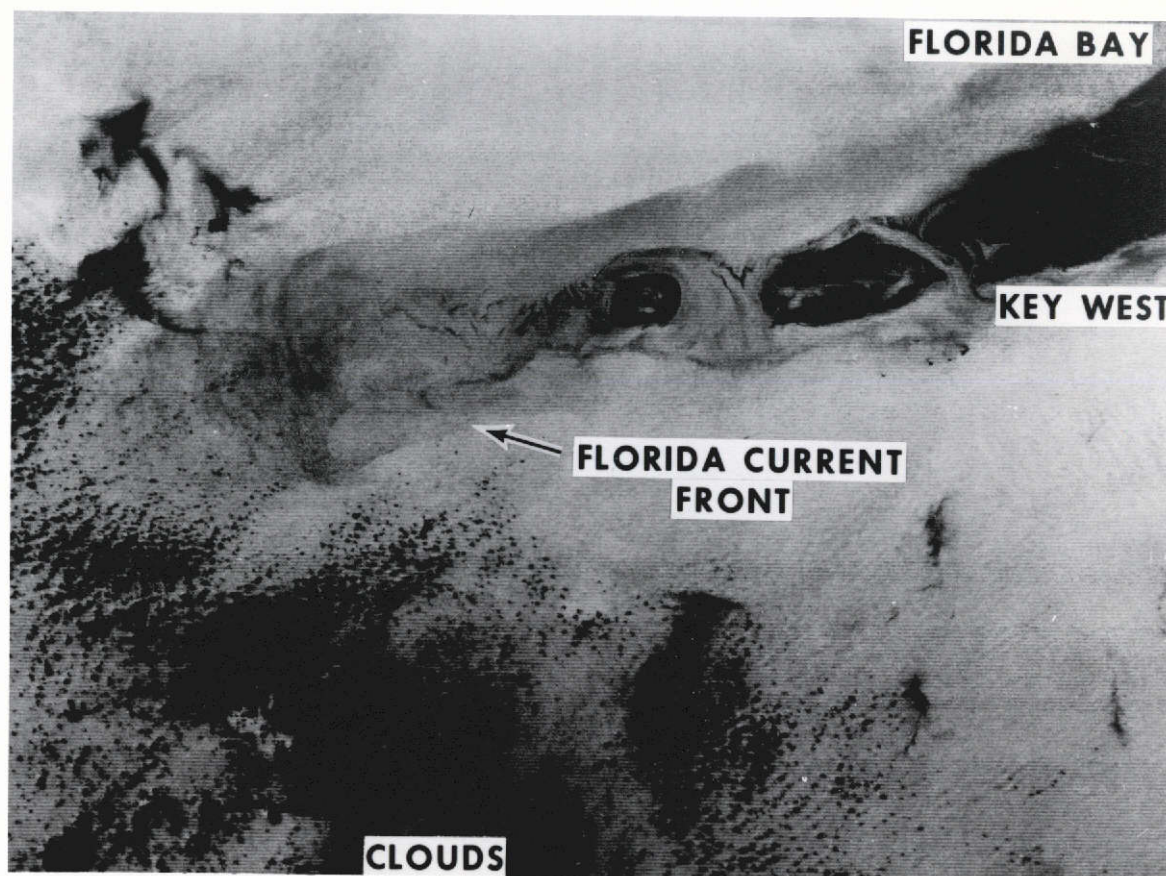
Figure 7. Negative print of computer enhanced ($7 \leq DN \leq 15$; $n = 2$) MSS 5 image of Marquesa Key and Key West (ERTS ID 1099-15293). Change in radiance southwest of Marquesa from dark to light marks the ship located boundary between the higher intensity Florida Bay water and the lower intensity Gulf Stream. Bottom depth is in excess of 100 meters and thus does not contribute to the radiance. Horizontal distance across the image is 135 kilometers.
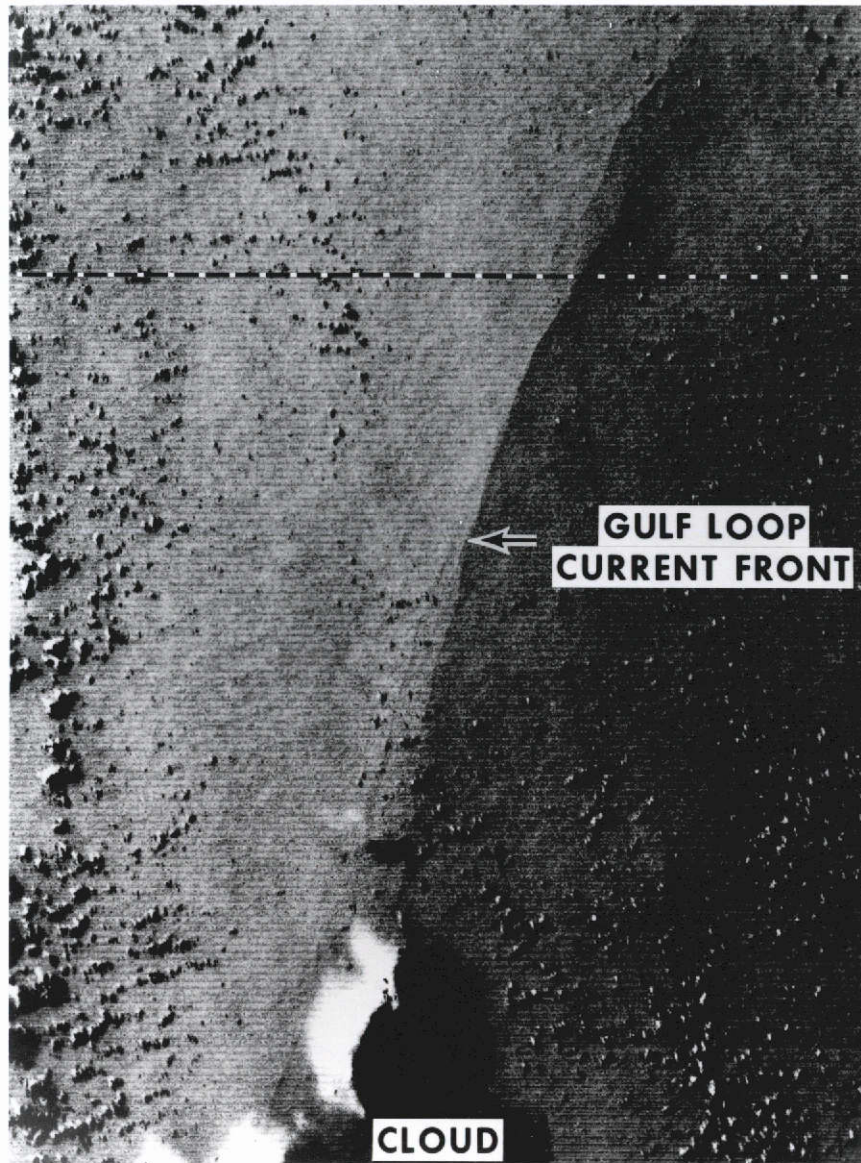
Figure 6. Negative print of computer enhanced ($9 \leq DN \leq 13$; $n = 1$) MSS 5 image of the cyclonic boundary of the Gulf Loop Current. Surface vessel track confirmed the location of the current to be the darker shade (higher radiance) region on the right hand side of the image (ERTS ID 1065-15411). Scanline plot in figure 5 horizontally passes through the middle of the scene. Horizontal distance across the image is 90 kilometers.

For example, Ross and Cardone (1972) observed that with 15 m s^{-1} winds, 10% of the surface of the sea is covered with white caps, and white caps reflect approximately 90%. If reflectance of the ocean is assumed to be 5% in the absence of white caps and 10% of the sea is covered with white caps, then reflectance is R = 5% (.9) + 10% (.9) = 13.5% or 270% higher than without white caps.

SOME THEORETICAL CONSIDERATIONS

At this point it is useful to consider in detail the processes contributing to the radiance spectrum $N(\lambda)$ at the position of the satellite. Solar radiation incident at the top of the atmosphere is absorbed and scattered in the atmosphere. Some radiation is scattered back into space without striking the ocean contributing a radiance $N_s(\lambda)$ at the satellite. The rest (which is not absorbed) will interact with the ocean. This interaction can yield upwelling radiance above the ocean in three ways: 1) specular reflection from the surface; 2) diffuse reflection from foam (bubbles) on or just beneath the ocean surface; and 3) the diffuse reflection from water molecules and suspended particles in the water. Of these the first two phenomena are closely related in that they depend on the sea state, while the third source of radiance is essentially independent of sea state. The specular reflectance from the rough ocean surface can be computed by the methods of Cox and Munk (1954) in terms of the wind speed and incident radiance distribution. The diffuse reflectance from white caps can be approximately accounted for by assuming they are "white", Lambertian, and have an albedo of 1 so that they contribute uniform

- 21 -

upwelling radiance just above the surface given by

$$H_0(\lambda) \frac{f}{\pi}$$

where f is the fraction of the scene covered by the white caps and $H_0(\lambda)$ the irradiance incident on the sea surface. The third source of radiance, that from beneath the surface, is the most difficult to compute and will be discussed in detail below. We can write the radiance at the satellite as

$$N(\lambda) = N_S(\lambda) + \gamma(\lambda)N_{ss}(\lambda) + \alpha(\lambda) N_d(\lambda) \tag{2}$$

where $N_{ss}(\lambda)$ is the contribution at the surface due to reflection from the surface and white caps, N_d is the diffuse radiance just above the surface due to photons that have penetrated the ocean, $\alpha(\lambda)$ and $\gamma(\lambda)$ are atmospheric transmittance factors for N_d and N_{ss}. $\alpha(\lambda)$ and $\gamma(\lambda)$ are in general not equal since the radiance distribution (variation with angle) of N_{ss} and N_d are different. It is possible for photons to be reflected from the surface, backscatter from the atmosphere into the ocean, and scatter back into the atmosphere. Photons which do this we consider to be a part of N_d. It should be stressed at this point that $N_d(\lambda)$ in the above equation is the only source of radiance that contains information about conditions beneath the sea surface such as the concentration and composition of suspended particles and dissolved organic material. A thorough understanding of the dependence of $N_d(\lambda)$ on the basic optical properties of the water and its constituents is required in order to obtain quantitative information about the constituents of the ocean from measurements of $N_d(\lambda)$.

The remainder of this section is devoted to relating $N_d(\lambda)$ to these optical properties. We shall assume that the radiance distribution incident on the sea surface is given, and that the radiance is transmitted from the ocean to the satellite in a known manner given by $\alpha(\lambda)$ and $\gamma(\lambda)$ in equation 2. This reduces the problem to that of taking a known down-welling radiance distribution just above the sea surface, and computing the distribution (just above the surface) of the upwelling radiance. As mentioned above, radiant energy interacting with the ocean can be absorbed by water, suspended particles, and dissolved organic material commonly called yellow substance with absorption coefficients a_w, a_p, a_y respectively and scattered by the water and particles with scattering coeffi-cients b_w and b_p (scattering by the yellow substance appears to be negligible). The total attentuation coefficient, c, for these interactions is given by

$$c = c_w + c_p + c_y \tag{3}$$

where
$$c_w = a_w + b_w,$$
$$c_p = a_p + b_p, \tag{4}$$
$$c_y = a_y$$

are the beam attenuation coefficients of the water, particles, and yellow substance. The scattering is further characterized by the phase function, $P(\theta)$, which relates to the intensity of radiation, $dJ(\theta)$, singly scattered from a small sample volume, dv, when illuminated by an incidence irradiance,

H_0, through

$$P(\theta) = \frac{dJ(\theta)}{(H_0 dv)b}$$

(5)

$$2\pi \int_0^\pi P(\theta) \sin\theta \, d\theta = 1.$$

The total phase function for water and particle scattering is

$$P(\theta) = \frac{(b_w P_w(\theta) + b_p P_p(\theta))}{(b_w + b_p)}$$

where P_w and P_b are the phase functions due to water only and particles only respectively. It is convenient to further define the forward (F) and backward (B) single scattering probabilities by

$$B \equiv 1 - F$$

(6)

$$F \equiv 2\pi \int_0^{\pi/2} P(\theta) \sin\theta \, d\theta$$

and the single scattering albedo by

$$\omega_0 \equiv \frac{b}{c} \, .$$

(7)

Hence it is clear that

$$B = \frac{(b_p B_p + b_w B_w)}{(b_p + b_w)} \, ,$$

(8)

$$\omega_0 = \frac{(b_w + b_p)}{(a_w + a_p + a_y + b_p + b_w)} \, ,$$

(9)

and in general, $0 \leq \omega_0 \leq 1$.

It should be noted that all of the above quantities depend on wavelength (λ). The transfer of radiation in the ocean is governed by the radiative transfer equation which has been discussed in detail by Chandrasekhar (1960) and Preisendorfer (1965). Gordon and Brown (1973) have computed the diffuse reflectance (upwelling irradiance/incident irradiance) just above a flat homogenous ocean as a function of its optical properties by a Monte Carlo technique. Using a combination of the parameters which arise naturally from the quasi-single scattering model (Gordon 1973), Gordon, Brown and Jacobs (in preparation) show that the diffuse reflectance (R_d) can be written

$$R_d = 0.179x + 0.0510x^2 + 0.1710x^3 \tag{10}$$

where
$$x \equiv \frac{B\omega_0}{(1 - \omega_0 F)} .$$

R_d is to first order independent of the distribution of the incident irradiance. It should be emphasized that the above equation does not include the irradiance specularly reflected from the sea surface or white caps, i.e. R_d is the contribution to the reflectance from photons which penetrate the surface and are multiple scattered back into the atmosphere. Preliminary computations (Gordon and Brown unpublished) indicate equation 9 is also valid for a moderately rough surface. The radiance distribution above the sea surface (due to photons scattered out of the ocean) is only weakly dependent on ω_0, and B'in the same fashion as R_d. Hence, it is sufficient to study the influence of the optical properties of the ocean on R_d alone.

Equation 9 shows that the important oceanic parameters are ω_0 and B, and so the observed reflectance spectrum, $R_d(\lambda)$, can be explained entirely through a knowledge of $\omega_0(\lambda)$ or $B(\lambda)$. Conversely, under optimum conditions, only $\omega_0(\lambda)$ or $B(\lambda)$ can be deduced from R_d and then only if one of these quantities is already known. The situation appears quite depressing when it is realized that $\omega_0(\lambda)$ is only imperfectly known even for pure water, and to our knowledge there are no measurements of $B_p(\lambda)$ and $\omega_0(\lambda)$ for various kinds of suspended particles. Hence, at the present time it is difficult to interpret $\omega_0(\lambda)$ and $B(\lambda)$ even if both could be extracted from $R_d(\lambda)$ measurements. This underscores the necessity of laboratory experimentation to determine these optical properties for various ocean constituents such as marine phytoplankton, and suspended mineral particles, for adequate interpretation of oceanic "color". If the optical properties of the constituents are known, then it is theoretically possible to determine their concentrations through observations of $R_d(\lambda)$ as is discussed in several examples below.

We shall now examine a particularly simple problem of interpretation, that of determining the concentration of suspended material in the absence and presence of yellow substance. The particles are assumed to be non-absorbing, and their scattering coefficient is assumed to be independent of wavelength [cases where $b_p = $ (const.) λ^{-n} with $n \leq 1$ have also been investigated and yield results not dramatically different from the $n = 0$ case]. These calculations will not apply at all to locations with particles containing absorbing pigments such as phytoplankton in the water, since Mueller (1973) and Gordon (1974) have shown that scattering from

such particles varies strongly with wavelength near the pigment absorption bands.

In order to use equation 10, $B(\lambda)$ and $\omega_0(\lambda)$ in equations 8 and 9 must be determined. We shall follow Tyler, Smith and Wilson (1972) and use for b_w and B_w values experimentally computed for sea water continuously filtered for 18 hours (Petzold 1972), rather than theoretical computations of these quantities for pure water. We do not feel comfortable with this, however, on the above basis they have estimated the absorption spectrum of "clear natural water", and since we use their $a_w(\lambda)$ spectrum, this assumption is essential for consistency. It is thus assumed that $B_w = 0.1462$ and $b_w = 0.008 m^{-1}$ at 550 nm, so

$$b_w = 0.008 \left[\frac{550}{\lambda}\right]^4 m^{-1}$$

To find B_p, Petzold's measurements of $P(\theta)$ from the Tongue of the Ocean (TOTO), San Diego Harbor (SDH), and Off Shore California (OSC) at 530 nm have been used. Assuming the above for B_w and b_w, the contribution from water is subtracted yielding the B_p values listed in Table 1 (ω_0 is given in the parenthesis and ω_0 for filtered sea water at this wavelength is 0.136).

TABLE 1

Derived Values of B_p for the Indicated Locations

TOTO	SDH	OSC
0.0165 (.59)	0.0186 (.82)	0.00966 (.59)
0.0158 (.25)	0.0194 (.83)	0.00836 (.55)
0.0130 (.26)	0.0169 (.91)	0.00836 (.55)

From Table 1 it is clear that B_p not only varies considerably from one location to another, but also varies considerably for a single region. This is unfortunate in that for small ω_0, R_d is directly proportional to $\omega_0 B$, and ω_0 and B are then equally important in determining R_d for these cases. We shall assume that Table 1 gives the range of variation of B_p to be expected in natural waters, however this is probably not the case. Furthermore we will assume B_p (and B_w) is independent of wavelength.

Since a_p is taken to be zero, and the $a_w(\lambda)$ estimate of Tyler, Smith and Wilson is to be used, only $a_y(\lambda)$ remains to be considered. This is taken from Jerlov (1968) and parameterized by

$$a_y(\lambda) = a_y e^{0.0145(550-\lambda)}$$

where λ is in nm. Reasonably high concentrations of yellow substances in the open ocean have $a_y \simeq 5 \times 10^{-3} m^{-1}$ (i.e., near Galapagos Islands) however, a_y can be much larger in coastal regions.

Using the above and equation 10, we have computed $R_d(\lambda)$ called Reflectance (0,-) in the figures, as a function of b_p/b_w (proportional to the concentration of suspended particles) for various values of B_p and a_y. The results are given in figures 8 through 12.

Figure 8 shows the R_d for $\lambda = 550$ nm as a function of b_p/b_w and B_p. The linearity of R_d with b_p/b_w is to be noted. These results clearly demonstrate the importance in knowing B_p for a quantitative determination of the particle concentration from R_d (which is measured at the sea surface). Figure 9 shows spectra of Rd again for various values of b_p/b_w but now with $B_p = 0.0165$. These spectra have the same general shape as those observed by Tyler and Smith (1970) just beneath the surface in Crater Lake,
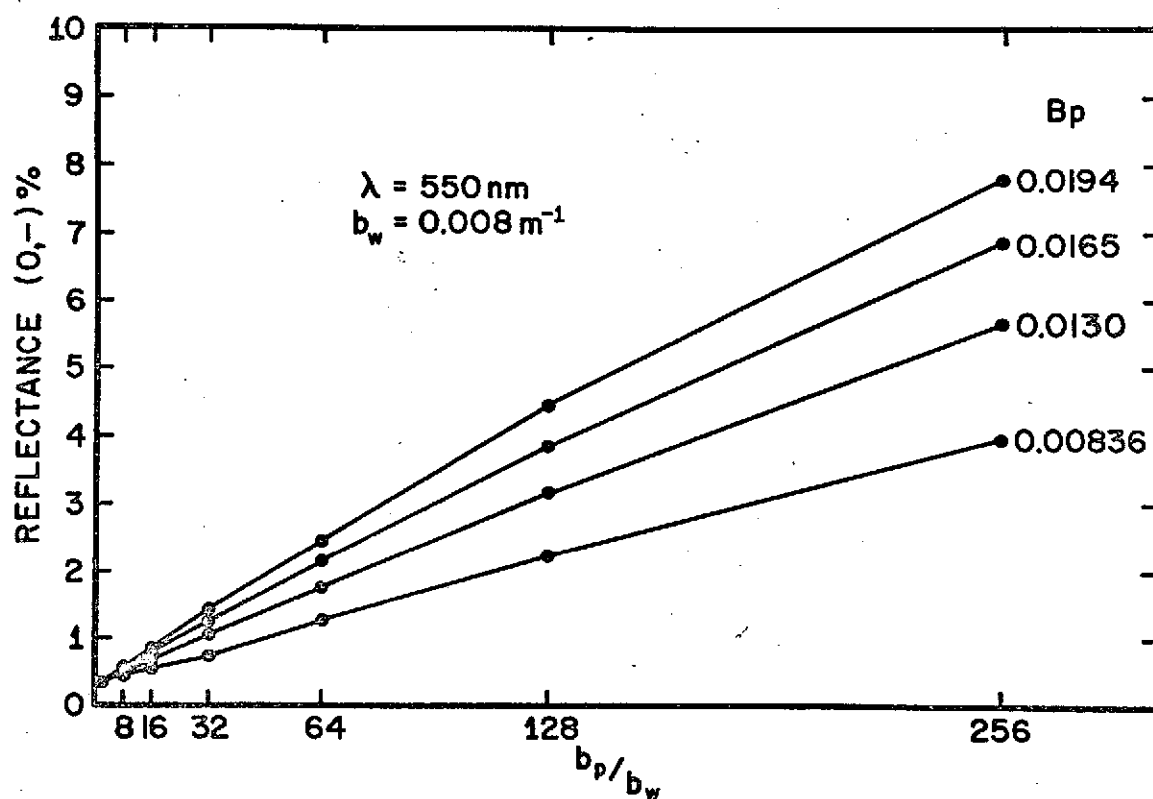
Figure 8. Computed reflectance in percent at the sea surface as a function
of the ratio of the particle scattering coefficient to the water
(only) scattering coefficient for 550 nm. The value of the
fraction of backscattered light due to particles (B_p) for each
curve is given on the right hand side.
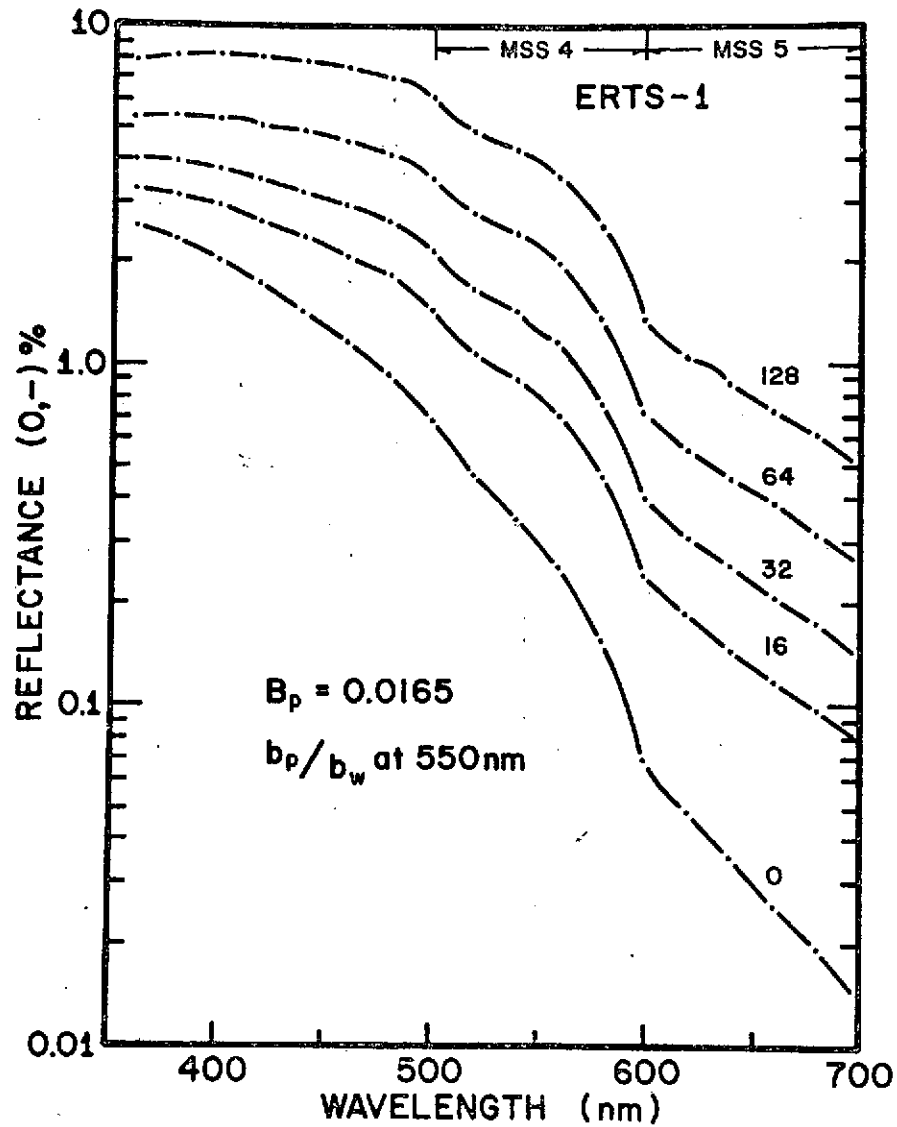
Figure 9. Computed reflectance in percent at the sea surface as a function of wavelength for various values of the ratio of the particle scattering coefficient to the water scattering coefficient. Note the wavelength dependence in these spectra of changing the particle concentration only.

but are not in quantitative agreement even when the loss due to transmittance through the water surface is considered. Basically the difference is that quantitative agreement requires too large a value of b_p/b_w. This could be due to the value of B_p used, the fact B_p is assumed to be independent of wavelength, or inaccuracies in their estimated $a_w(\lambda)$ on which the present calculations are based. In any event the computations can be used as a guide for examining ERTS related data. Figure 10 shows the influence of yellow substance on the reflectance for the case with $b_p/b_w = 128$ and $B_p = 0.0165$. The major influence of the Gelbstoff (yellow substance) is to depress the blue region of the reflectance spectrum. All of these results are summarized in figures 11 and 12, where the reflectances have been integrated over the ERTS MSS channels 4 (figure 10) and 5 (figure 12) for various B_p and a_y as a function of b_p/b_w. It is seen that the Gelbstoff influences the reflectance in MSS 4 only at very high concentrations (for the open ocean) and essentially plays no role in the MSS 5 reflectance. Therefore, for suspended particle concentrations, it appears that MSS 5 is best with MSS 4 only slightly degraded by the dissolved organic materials. It should be emphasized again that the above discussion refers only to the case of no phytoplankton (chlorophyll)!

We now turn to the problem of estimating b_p/b_w or some related quantity from satellite observations. Since the above calculations are only for the case of negligible phytoplankton (chlorophyll) concentrations, we must find criteria from which to choose which ERTS channels will satisfy this constraint. Also unless only MSS 5 is used we expect Gelbstoff to
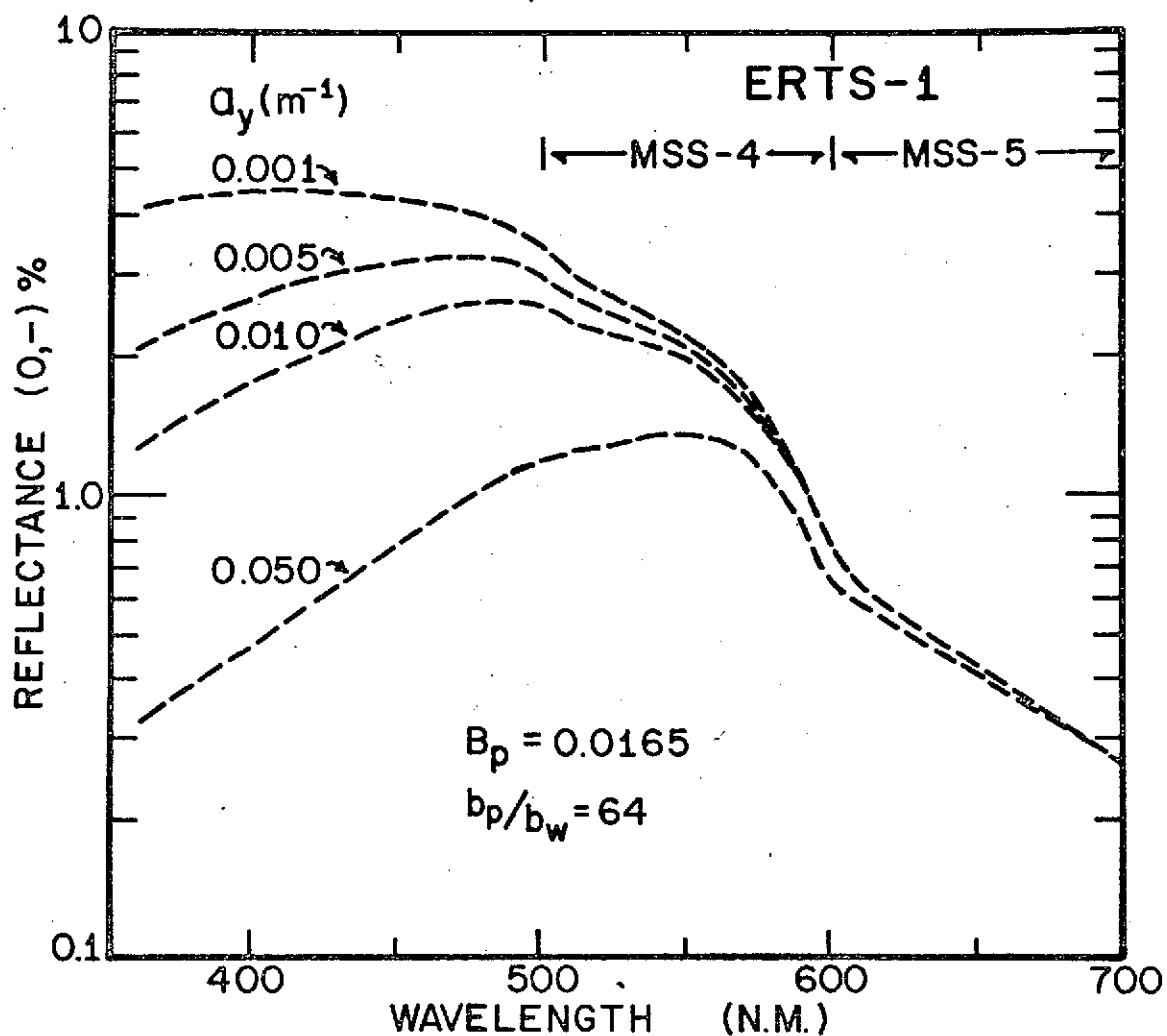
Figure 10. Computed reflectance spectra, in percent, at the sea surface. The ratio of the particle to water scattering coefficients (b_p/b_w) and the fraction of backscattered light are 128 and 0.0165 respectively. Values of the absorption coefficient due to yellow substance (a_y) are listed on the left hand side. Note the shift of the spectral peak to longer wavelengths with increasing a_y.
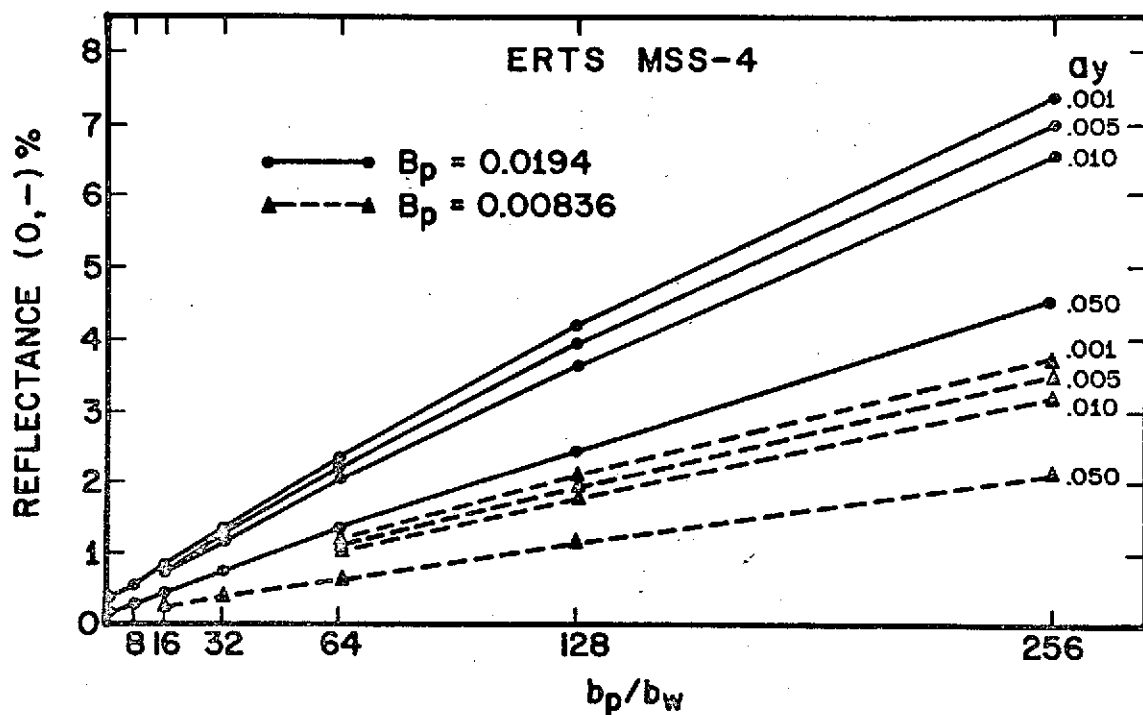
Figure 11. Computed reflectance in percent at the sea surface as a function
of the ratio of the particle to the water scattering coefficients
integrated over the spectral response of the MSS 4 filter (0.5 -
0.6 μm). Values of the absorption coefficient due to yellow sub-
stance (a_y) are listed along the right hand side. Note the lin-
earity depends on both a_y and the fraction of backscattered light,
(B_p).
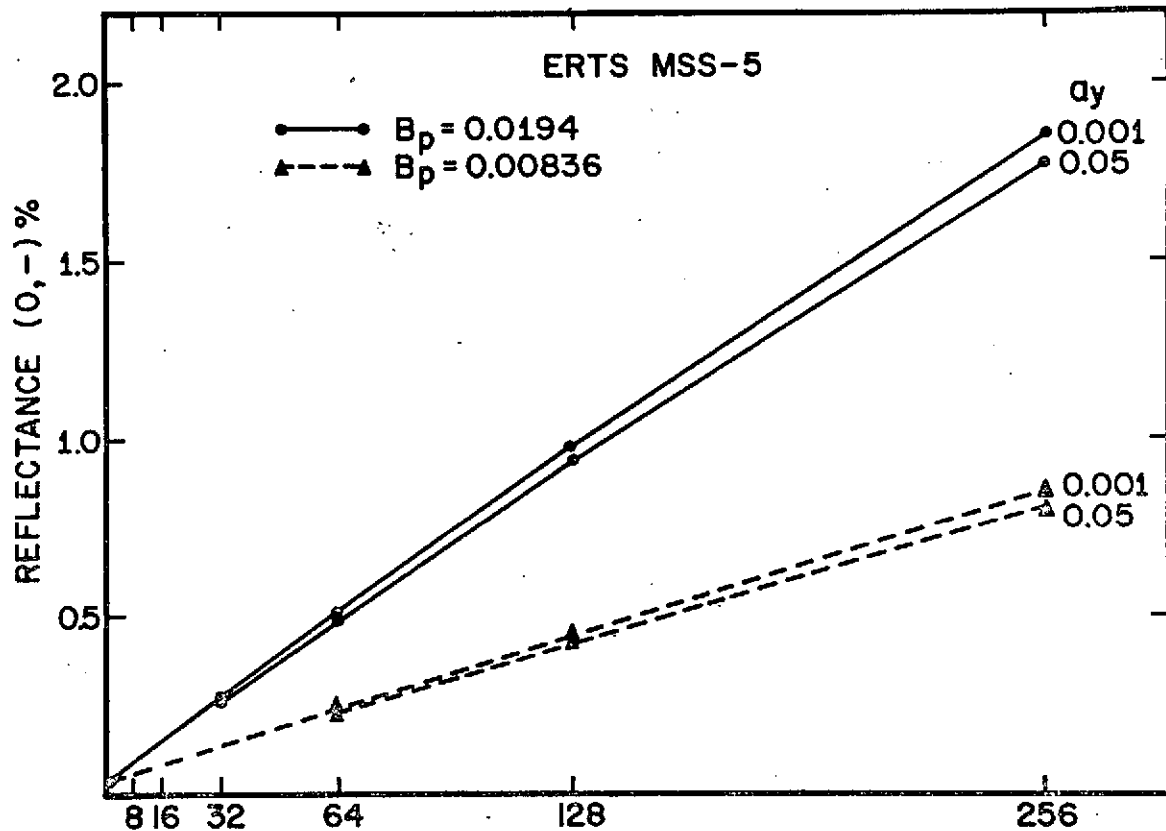
Figure 12. Computed reflectance at the sea surface, in percent, as a function of the particle to water scattering coefficient ratio, integrated over the response function of the MSS 5 filter (0.6 - 0.7 μm). Value of the absorption coefficient due to yellow substance (a_y) are listed along the right hand side. Note the linearity is not strongly dependent on a_y but only on the fraction of backscattered light, B_p.

be important especially in coastal regions where river runoff, etc., may be considerable. Furthermore there is the additional problem that the reflectance depends on B_p which is also unknown, as well as b_p/b_w. We have developed a method which partially overcomes some of these problems. Considering the radiances observed in MSS 4 and 5, we have approximately

$$N_4 = \alpha_4 N_{d_4} + \gamma_4 N_{ss_4} + N_{s_4}$$

$$N_5 = \alpha_5 N_{d_5} + \gamma_5 N_{ss_5} + N_{s_5}$$

(11)

where α_i and γ_i (i = 4, 5) are the fractions of N_{d_i} and N_{ss_i} (measured at the sea surface) that reach the sensor. It is assumed that α_i and γ_i are constant over an ERTS frame (if they vary in a known way, their influence is easily accounted for and will not be discussed further). Now from the theory

$$N_{d_4} = k_4 \frac{b_p}{b_w}$$

$$N_{d_5} = k_5 \frac{b_p}{b_w}$$

(12)

where k_4 and k_5 are essentially independent of b_p/b_w, but depend directly on B_p. Taking the horizontal gradient, ∇_H, of equation 11 using equation 12 we find

$$\nabla_H N_i = k_i \alpha_i \nabla_H \left(\frac{b_p}{b_w} \right) + \gamma_i \nabla_H N_{ss_i}$$

(13)

since N_{s_i} is nearly constant over a frame ($\nabla N_{s_i} = 0$). The last term in equation 13, $\nabla_H N_{ss_i}$, is the horizontal gradient of the reflected radiance

- 35 -

from the sea surface. This is nearly zero everywhere except where

the sea state changes dramatically with horizontal distance (for example

in figure 6). Nearly everywhere on the frame then, $\nabla_H N_{ss_i} = 0$, so

$$\frac{\nabla_H N_4}{\nabla_H N_5} = \frac{k_4 \alpha_4}{k_5 \alpha_5} \tag{14}$$

Again α_4/α_5 is constant (or slowly varying) over the scene; so almost

everywhere in the frame, variations in $\nabla_H N_4/\nabla_H N_5$ are the result of var-

iations in k_4/k_5. Now if B_p is constant, or if the "mean" B_p is constant

in each wavelength band, this would imply that essentially only the con-

centration of scattering particles varies over the frame, i.e. not the

nature of particles or their size distribution. In this case, k_4/k_5

would be constant. Hence essentially k_4/k_5 will vary, if the nature or

size distribution of the particles varies over the frame (B_p changes),

or if the Gelbstoff concentration varies considerably over the frame,

which would force k_4 to vary independently of k_5. Thus if we find

$$\frac{\nabla_H N_4}{\nabla_H N_5} = \text{Const} \tag{15}$$

it is reasonable to expect that only the particle concentration changes

over the frame. In this case

$$\nabla_H N_4 \text{ or } \nabla_H N_5 \sim \nabla_H \text{ (particle concentration)} \tag{16}$$

Note here that these relations should also apply to scenes containing

phytoplankton if they are the dominant scatterers; but for mixtures of

phytoplankton and suspended white particles, one would expect equation 15 to be violated over a scene if the relative concentrations vary drastically. To reiterate, if 15 holds, probably only the particle concentration varies over the frame, and 16 can be used to measure the gradient of its concentration. Since B_p is unknown, the actual concentration is indeterminate without ground truth to better than a factor of two, since this is the assumed uncertainty in B_p. Several examples of the use of the above ideas for analysis of ERTS data are presented below.

DISCUSSION

Equation 16 was applied to MSS 4 and MSS 5 data in figure 13. This computer enhanced negative image of the Cape Hatteras region shows what appears to be large gradients in suspended sediment. The Gulf Stream apparently has entrained particles from Rayleigh Bay and is carrying them out to sea. Along the scanline shown we have computed

$$\frac{\partial}{\partial x} [N_4] = g\frac{\partial}{\partial x} [N_5] + h \tag{17}$$

where the least squares values for g = 0.38 and h = 0.00, and the linear correlation coefficient, r, is 0.66. The coefficient of determination, r^2, which is the ratio of the explained variation from the mean (by the least squares line) to the total variation, is 44%. Physically this means that this image may not be useful for determining particle concentrations because B_p, ω_0 (i.e. a_y), or b_p/b_w may be changing. The extent to which this holds true in natural waters is unknown; this will be
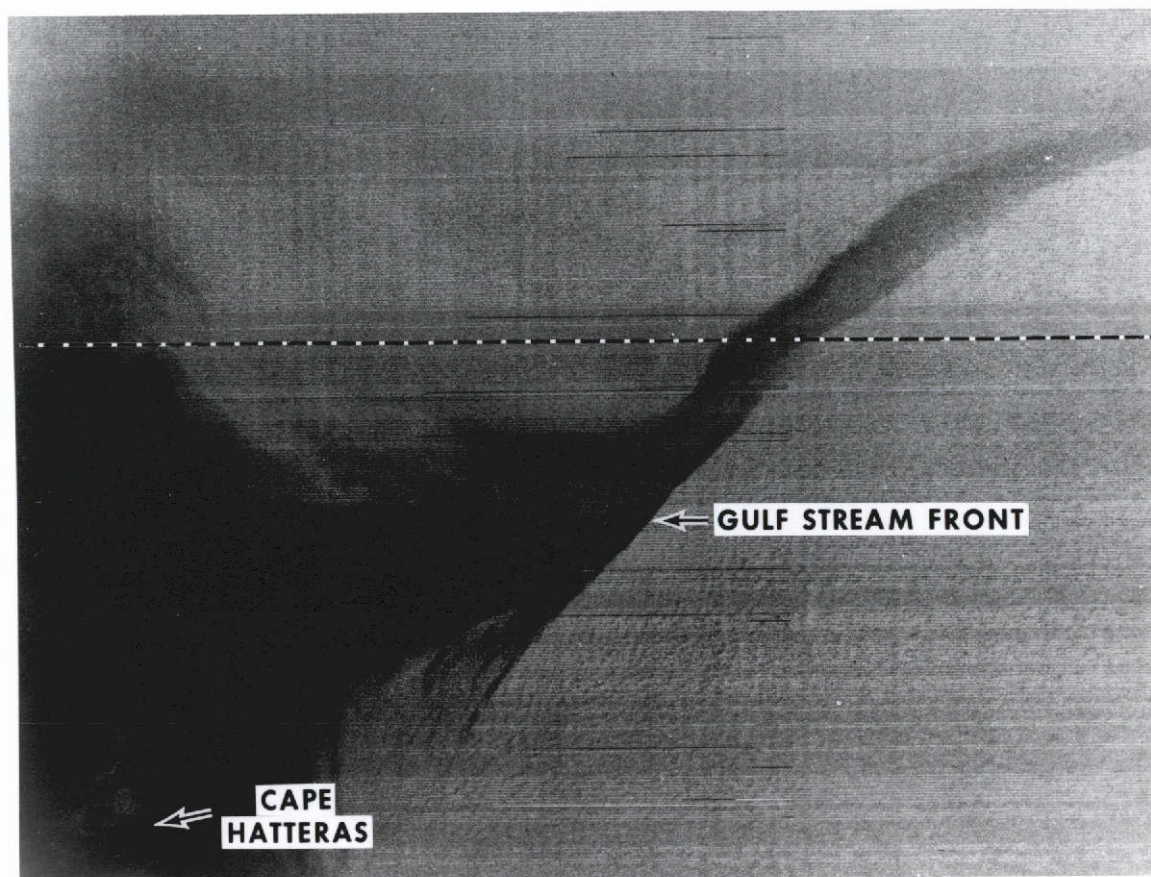
Figure 13. Contrast stretched (4 ≤ DN ≤ 12; n = 2) negative image of the ocean area offshore of Cape Hatteras (ERTS ID 1132-15042). The Gulf Stream can be seen as the bright area to the south of the entrained sediment from the coastal estuaries. The least squares fit of eq. (17) was done along a scanline north of the Cape and extending from nearshore, through the suspended sediment and into the current. Extensions of this plume were observed for 150 kilometers further east on other ERTS images. Horizontal distance across the image is 135 kilometers.

- 38 -

extensively tested in the New York Bight area where turbidity measurements are being made by NOAA vessels concurrent with ERTS transits. A plot of the gradients from figure 13 and discussed above is given in figure 14. Note that ∇_H MSS 4 follows ∇_H MSS 5 quite well in this low passed filtered version of equation 16.

The data of figures 9 and 10 can be compared to measurements of upwelling irradiance. Data given in figure 15 were observed using a 1/4-meter Ebert spectroradiometer from 3 meters above the surface; these observations were made during the time frame of figure 7 and represent the water types shown in that image. All spectra were carefully selected to represent the same downwelling irradiance, sea state, sun angle, cloud cover, and absence of bottom influence. Specular reflection due to waves were minimized by preselecting ten spectra with similar shapes. After digitizing the records, averages and standard deviations (σ) were computed at each wavelength; if values exceeded the average by 1σ, they were rejected and a new mean computed. Absolute values of the spectra are traced to NBS through the 2-meter integrating sphere at NASA's Goddard Space Flight Center.

As the chlorophyll-a concentration increases, the spectral peak shifts to longer wavelengths in similarity with the computed data in figure 10. This is not to say that the chlorophyll-a and the yellow substance produce quantitatively similar results; in general they will not. What it does imply is that the broad absorption bands in pigments such as chlorophyll and Gelbstoff at shorter wavelengths (≤ 600 nm) produce qualitatively similar effects in the spectra. When other factors are equal, increasing the concentration of pigments will cause a
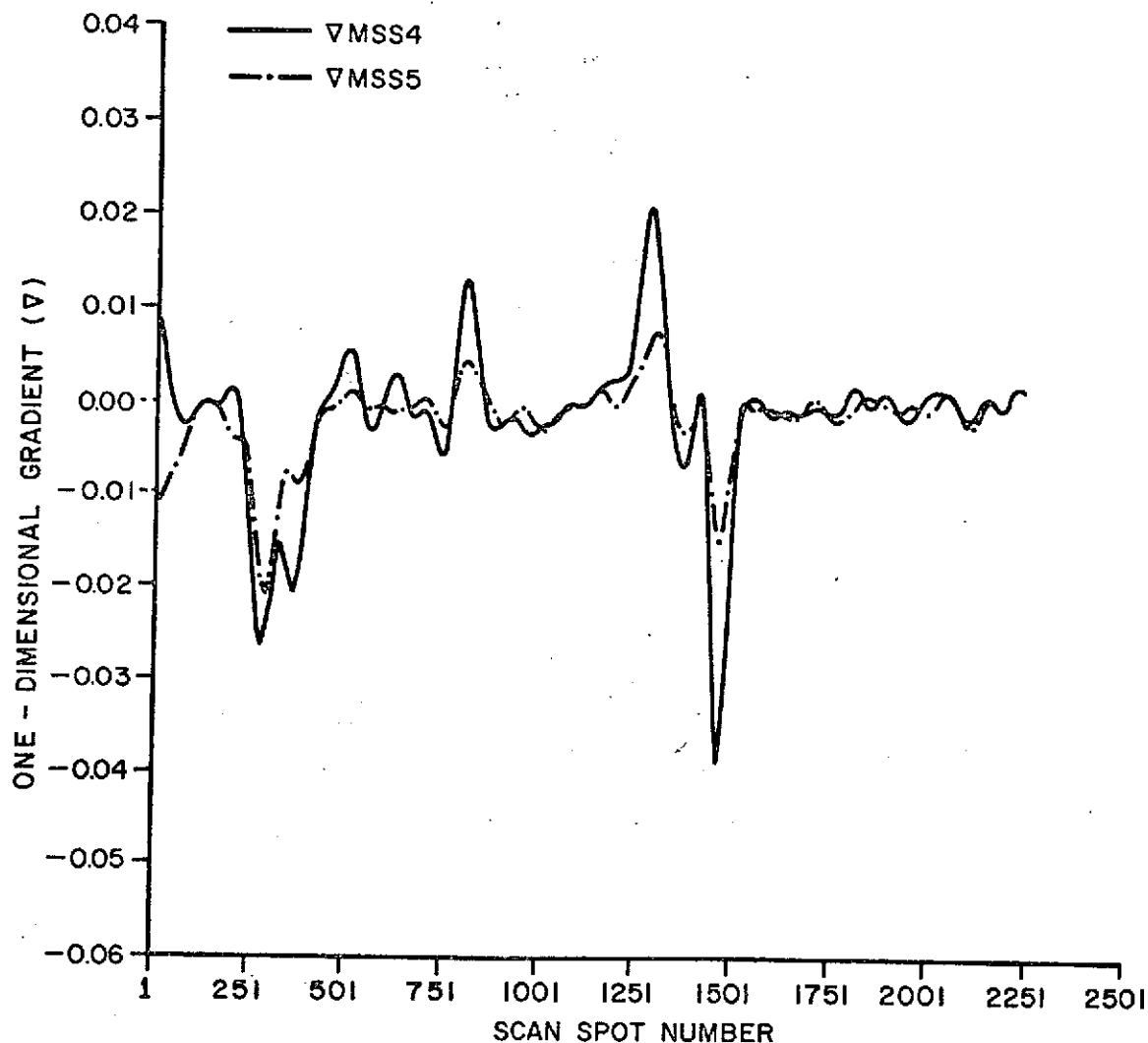
Figure 14. One-dimensional gradient of MSS 4 (solid line) and MSS 5 (broken line) along the dashed line in figure 13. The scan spot numbers along the abscissa refer to the data points in the original computer compatable tape. A low pass filter was applied to the gradient before plotting in order to reduce high (spatial) variability.

decrease in the radiance in MSS 4 only.   In nature however, such as in a plankton bloom or in a river plume, increased amounts of chlorophyll are normally accompanied by increased particle concentrations (organisms which contain the chlorophyll) as well as yellow substances (decay products of the plankton), and increased amounts of "white" suspended particles in the river plume case.   The radiances in MSS 4 and 5 will in these cases vary in a manner which will depend again on the relative concentration of the constituents, and since a and b vary almost independently, the reflectance signature, which depends on $\omega_0(\lambda)$ and $B(\lambda)$ is not unique and can be unraveled only when the variation of the optical properties of the individual components with wavelength is known.

As an example of this, the spectra given in figure 15 were integrated over the MSS 4, MSS 5, and MSS 6 filter functions.   A series of numerical tests were then made of ratios, differences, and sums to see if the three water types could be distinguished at the sea surface.   It was quite easy to distinguish on the basis of such calculations between the Gulf Stream waters and the coastal waters, and between the coastal waters and the plankton bloom; however it was not possible to distinguish between the Gulf Stream and the plankton bloom.   This suggests, as the theory implies, that for these data the ratio test (MSS 4/MSS 5) is not likely to be successful in specifying the chlorophyll-a concentration. Further, since the sea surface component, N_{ss}, (λ), spectrally alters $N(\lambda)$, numerical tests (ratios, differences, etc.) are invalid indicators of oceanic properties.   Theoretically, the signal of a differential radiometer (Arvesen, 1972) is subject to such variation in ω_0.   If it
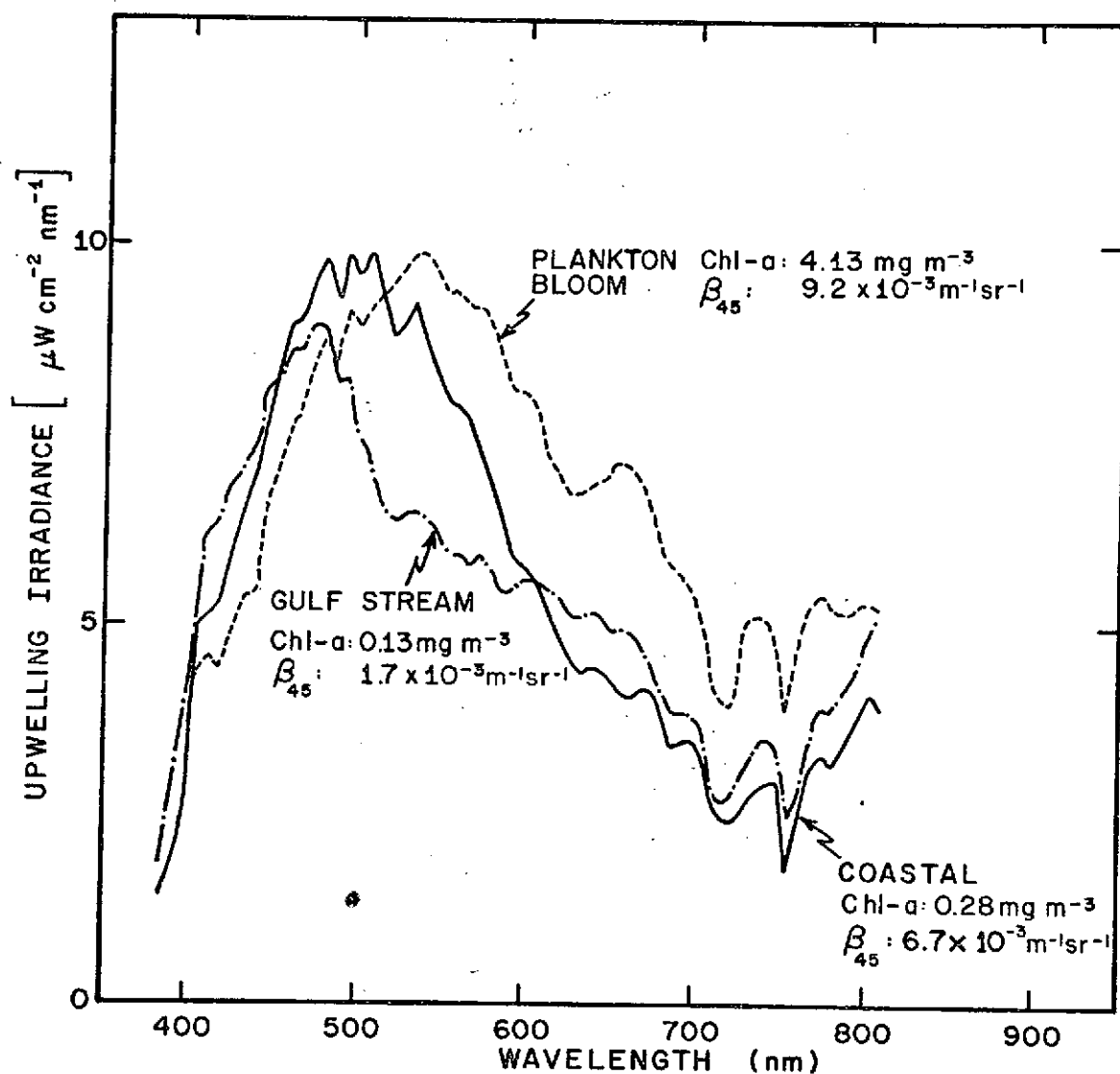
Figure 15. Observed upwelling spectral irradiance in the Gulf of Mexico, November 1972. The three spectra represent typical observations during the time series, and show the shift of the dominant wavelength to larger values with increased surface chlorophyll-a. The volume scattering function $\beta(45)$ is for blue (436 nm) light.

is fortuitous that ω_o always varies in the ocean such that $R(0,-)_{523}$ is constant (Duntley, 1972), then a dual channel instrument will work in the absence of sea state changes.

The solar spectrum is fairly flat in the visible region ($H(0,-)_{450}/H(0,-)_{700}$~1.3). Hence, higher sea states, which reflect high percentages of white light, proportionally add more long wavelength energy to the upwelling irradiance. In terms of a chromaticity diagram, this means that the purity changes but not the dominant wavelength. To correct for sea state a channel in a multispectral scanner near 1 µm appears useful. At this wavelength there is a maximum in the attenuation coefficient of pure water (i.e. $\omega_o \rightarrow 0$), a maximum in atmospheric transmissivity, and the influence of chlorophyll seems low.

Probably the most efficient method of determining the concentration of the constituents in the ocean will be to compare theoretical and experimental spectra, adjusting the constituent concentrations in the theoretical spectra until agreement is found. This of course requires a basic understanding of the optical properties of the constituents which can be derived only from careful in situ and laboratory experiments. It seems that at the present time much energy and money is being expended to try and use optical methods to locate and study materials with nearly unknown optical properties suspended or dissolved in a medium with only poorly known optical properties. This must be overcome before significant progress can be made.

An interpretation of oceanic observations from ERTS is given in figure 16 which is a computer enhanced MSS 6 negative image of southeastern
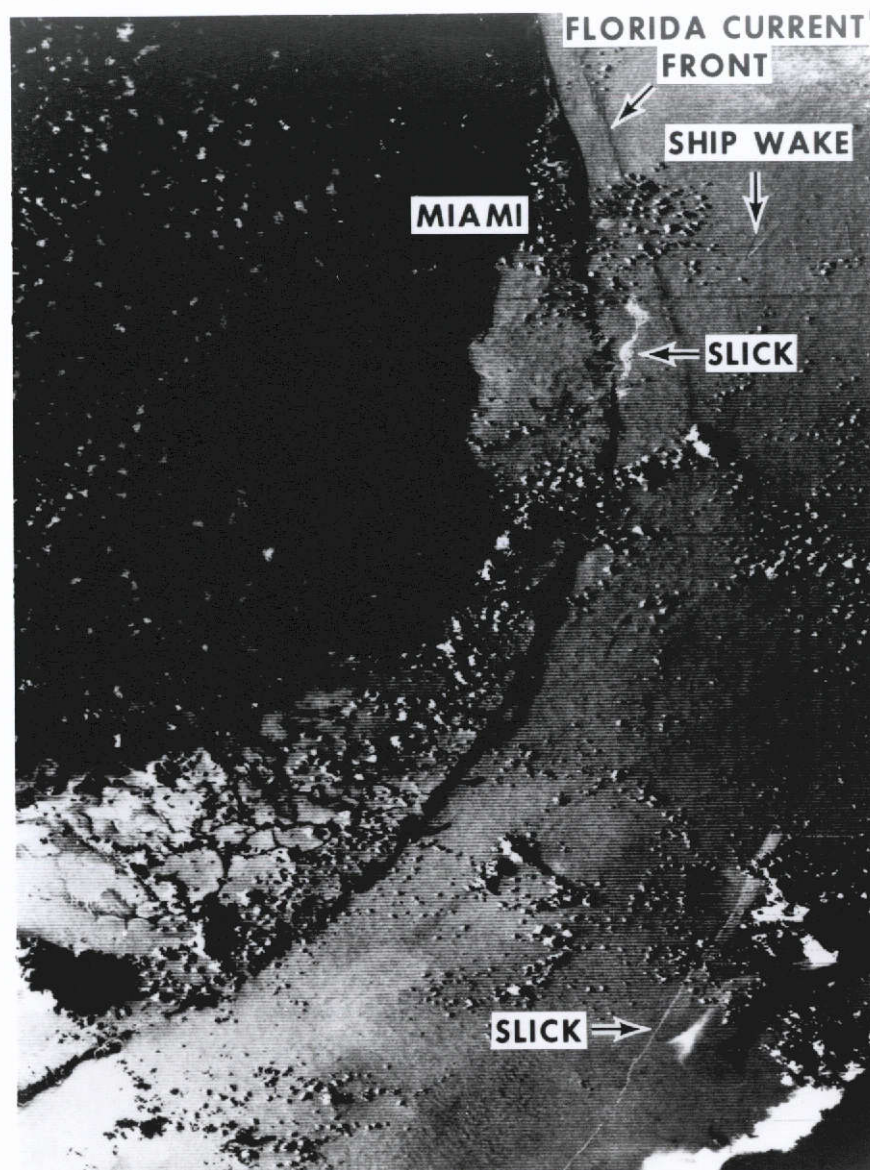
Figure 16. Negative print of computer contrast stretched ($7 \leq DN \leq 15$; $n = 2$) ERTS image of South Florida (ERTS ID 1026-15230). The Florida Current can be seen as a line of dark lineation parallel to the coast; bottom is essentially invisible in this MSS 6 scene. A ship can be seen by its characteristic V-shaped wake just offshore of Miami Beach. Possibly the Virginia Key sewer outfall area can be observed by its low reflectance due to an organic slick. Horizontal distance across the image is 90 kilometers.

Florida. The dark lineation parallelling the coast in the upper portion of the image is a zone of high reflection caused by locally increased N_{ss} along the edge of the Florida Current. The increase in surface reflectance is probably caused by surface wave interaction with the cyclonic boundary and is not bottom influence. This further explains the edge effect and supports the discussion on the local dependence of $\nabla_H N$ on $\nabla_H N_{ss}$ only given above. Another example of the dominance of N_{ss} is the bright slick areas (low N) off the Virginia Key sewer treatment plant. This is probably caused by the dampening of the glitter causing capillary waves in the oil film associated with the organic slick. The slick, which has drifted south past the popular Key Biscayne beaches, offers an explanation of the narrow lineation off shore in the Florida Straits: a passing oil tanker heading south which is pumping her bilges would cause a similar feature on the image. Thus ERTS could be useful in patrolling coastal waters for such illegal acts which affect the near-shore water quality.

NEARSHORE OCEANOGRAPHY

The New York Bight is currently the subject of an intensive program of marine ecosystem analysis (MESA) by NOAA. This program provides extensive opportunity to relate basic oceanographic observations to the observed satellite radiances. Cruises by NOAA research vessels are being made in synchronization with ERTS transits. The transmittance data given in figure 10 were collected over a several day period nearly centered on the day of transit.

Data can be smoothed before contouring in an effort to remove excessive noise and high wavenumber variability. This is accomplished by convolving a boxcar smoother kernel (SK) with the data matrix (DM)

$$SM = \frac{1}{j \times k} \sum_j \sum_k DM(j,k) \qquad (18)$$

to produce a smoothed matrix (SM).

Distinction should be made between smoothing and filtering. Smoothing in sample number space is defined as convolution with a boxcar filter kernel. Filtering in sample number space is convolution with a kernel which is the Fourier transform of a gate function from sample interval space. (Spectrally, sample number space is analogous to time, and sample interval space is analogous to period.) Smoothing is a form of filtering, but it employs a kernel that has undesirable side bands which can adversely affect the output.

In order to analyze the frequency characteristics of ERTS data, power spectra were computed along and normal to several scanlines in an oceanic region. Power spectra for data along a scanline (solid) and normal to scanlines (dashed) are given in figure 17; 600 points and a Lanczos squared window were used to compute these results.

Both power spectra have the shape typical of the geophysical continuum, i.e., increasing power with increasing sample interval. However, the energy in the along scanline plot is generally higher than across the scanline. Strong (1973) argued that ERTS data have sunglint at the larger nadir angles toward the solar specular region. That notion is supported in these power spectra, since the energy at large sample intervals

is higher along the scanline (oriented toward the specular region) than across scanlines (which is quasi-parallel to the specular region). The large amplitude spike in the across scanline power spectrum of figure 17 at every sixth sample is not observed in the along scanline power spectrum. This spike is due to the so-called "six-line banding" caused by the use of six-detectors in the MSS.

Many other power spectra were computed from different scenes and different spectral bands. There is a great deal of variability in the results because power spectra are very sensitive to the data chosen. Thus any conclusions based on Fourier estimates must be carefully viewed in light of the particular sample and judiciously applied to the ensemble.

From study of representative power spectra such as these, a filter can be designed which will effectively eliminate undesired variations and noise. The Lanczos squared low pass filter used in this study is designed to eliminate the six-line banding. It has a half power point (6 db down) at 10 samples and is 90% effective (20 db down) at 14 and 6 sample points. The filter kernel was chosen to have 19 x 19 elements. That size is a compromise based on sharp cutoff for a 10-sample interval and a practical amount of computer time.

Examples of different smoothing and filtering on the MSS 5 scene of the New York Bight are given in figure 18. The upper three panels are examples of using 3 x 3, 10 x 10, and 19 x 19 boxcar smoothers, top to bottom respectively. The lowest image is a filtered version using the 19-x 19 low pass kernel derived from analysis of figure 17. After convolving DM with the appropriate kernel, each image has been stretched
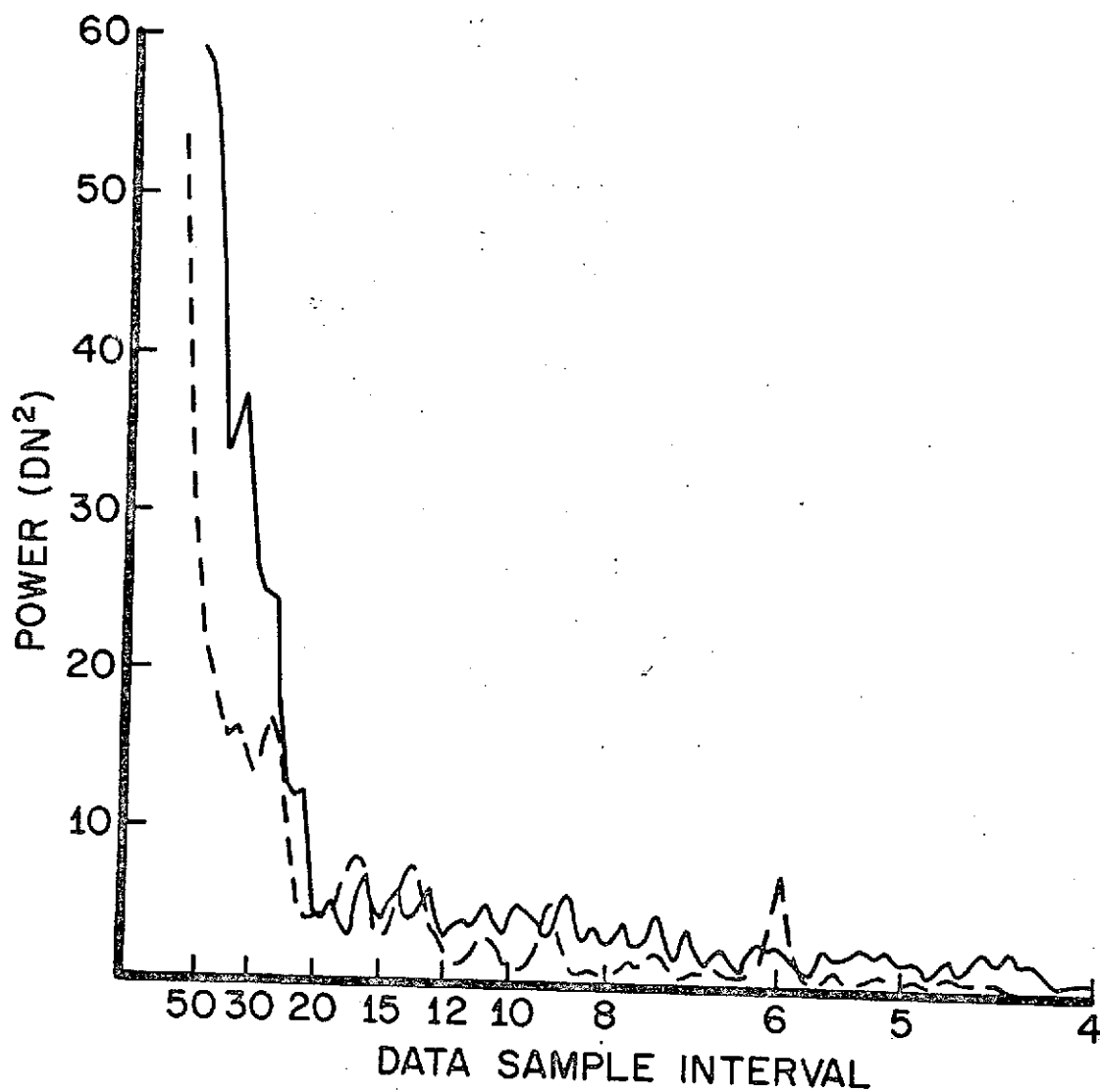
Figure 17. Solid line: Along scanline power spectra of oceanic data in MSS 5. Dashed line: Cross scanline power spectra of oceanic data. Power is in units of DN which has a radiance equivalent of mW $cm^{-2}sr^{-1}$.
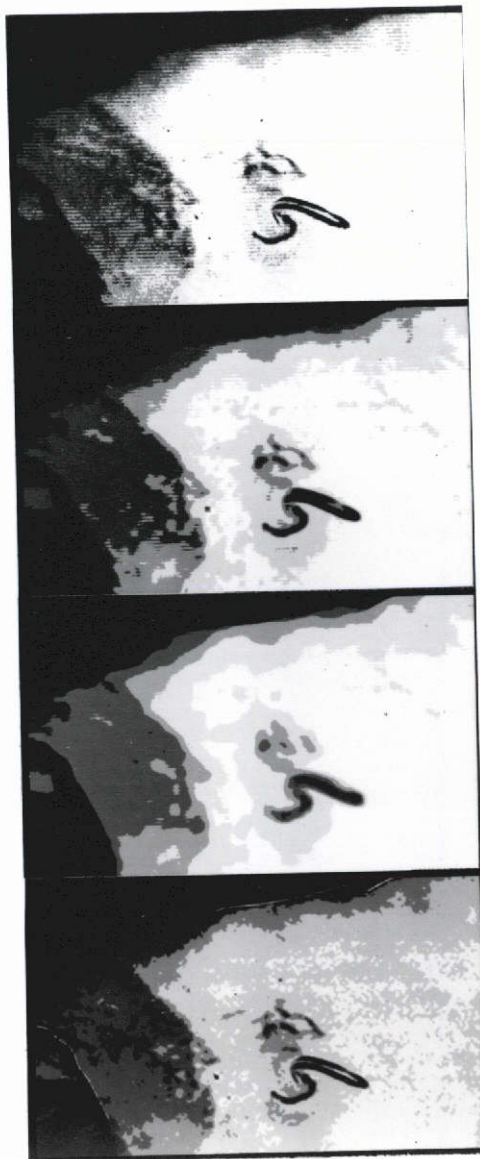
Figure 18.   Effects of smoothing and filtering on a portion of the data
in figure 2 [b].   Upper [a]; 3 x 3 boxcar kernel.   Second from
top [b]:   10 x 10 boxcar kernel.   Third from top [c]:   19 x 19
boxcar kernel.   Bottom [d]:   19 x 19 Fourier filter.   The
images are contrast stretched after convolution with the appro-
priate kernel.   Negative images.

for $7 \leq DN \leq 15$ and n = 2 by use of equation 1. Smoothing clearly reduces the overall variability in the imagery, but the six-line banding, which has the appearance of corduroy material in the original data, is still present even with a 19 x 19 smoothing kernel. More significant however, is the loss of detail when smoothing as compared to filtering. Detail in the waste dump site (V shaped feature) for example, is retained in the filtered matrix (FM) as is variability in the plume region. The filtered version eliminates variability in the scene with wavelengths less than about one kilometer.

Most of the contribution to filtering with a 19 x 19 kernel comes from the central 10 x 10 elements of the matrix. Comparing the 10 x 10 SK image (18 [b]) with the filtered version (13 [d]), note that variability is retained in the plume region, and east of the waste dump site for the same stretched DN range in FM, but not in SM.

Large sample internal variability, such as glitter, can be removed by high pass filtering. An alternate technique is to least squares fit a low order polynomial to the scanline and subtract out the contribution due to glitter. The least squares approach will not reduce the data matrix size due to convolution by a high pass kernel, however, the physical interpretation is more succinct when the data are viewed as being bandpassed in sample interval space.

The images in figure 19 are computer enhanced, filtered, MSS 5 data in the apex region of the Bight using equation 1 and the 19 x 19 filter kernel described above. Transmittance is defined as the percent transmission measured by a 10 cm attenuation meter in the surface layer
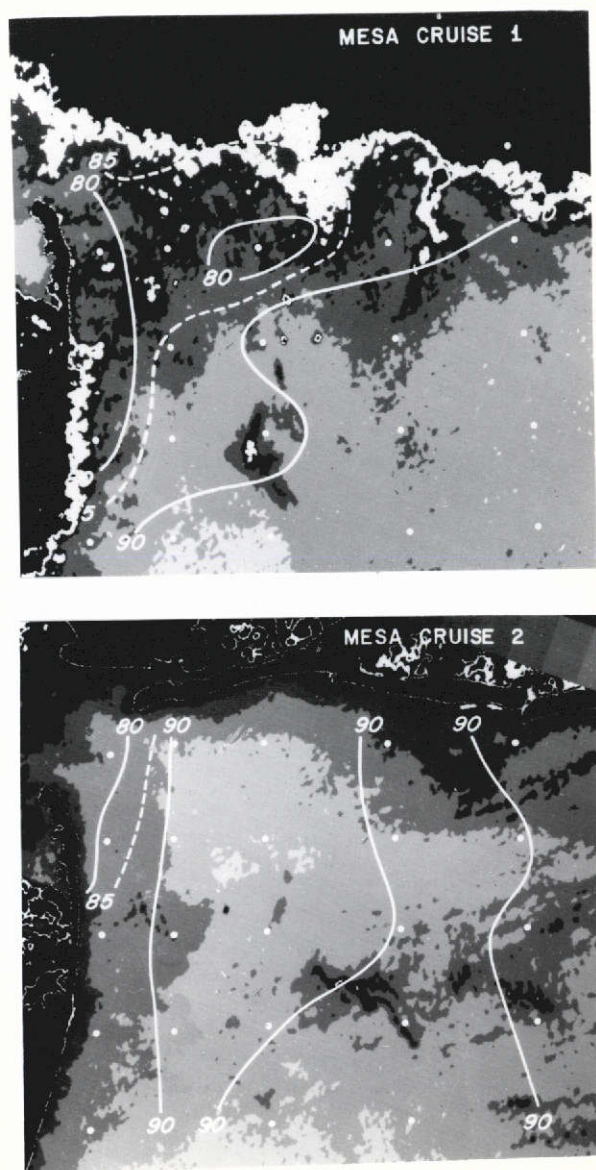
Figure 19.   Percent transmittance for the apex of the New York Bight.
Upper [a]:   29 August 1973 (ERTS ID 1402-15065) transit con-
trast stretched and filtered as in 8 [d].   Lower [b]:   16
September 1973 (ERTS ID 1420-15067) transit processed as in
[a].   Oceanographic stations used are located by dots.   Nega-
tive images.   Horizontal scale in each figure approximately
50 kilometers.

(upper meter) of the water column. Isopleths of transmittance were contoured from the ship data without regard to the satellite data for comparison purposes. A cursory inspection of figure 19 [a] reveals that the lower transmittance areas are also areas of higher radiance (negative image has high radiance black), but in 19 [b] this is not the case at all. The assignment of gray scales is arbitrary in each image.

If N_{ss} is constant (or high pass filtered out as required for the glitter problem) and if N_s is also constant, then changes in N are due to changes in N_d, i.e., changes in $R_d(0,-)$ as given by equation 10. In this equation, F, and hence B, depend on the particle concentration, the particle size, as well as the size distribution of the particles. Due to differential particle settling, changes in all three variables relating to the phase function $(\beta(\theta)/b)$ will occur in the Hudson River plume area. In addition, changes in ω_o can be expected here due to changes in the Gelbstoff distribution; these changes are independent of scattering and affect only absorption.

In addition to the variables affecting the reflectance, non-synopticity must be considered. Semidiurnal bidirectional tidal currents dominate the flow in the entrance to lower New York Harbor, but offshore the current regime is rotary, superimposed on a highly variable but generally net anticyclonic drift. Horizontal excursions for the rotary currents are less than 5 kilometers, and net drifts are approximately 6 cm sec^{-1} (~5 km day^{-1}). Winds were light and variable during these two passes so there was no significant effect on the surface circulation. The transmittance data therefore represent a quasisteady state situation

especially in the region of the waste dump site and along the coast away from the harbor entrance.

The inconsistency between observations of transmittance and ERTS radiances presented here is contrary to the conclusion by Klemas et al., (1973) in that these data show both theoretically and observationally that agreement hinges on the behavior of ω_0 and B. These experiments do support their conclusion on the usefulness of several analog enhancement techniques. Additional spectral studies of R(0,-) and the in situ variables are now in progress in the Bight area. These measurements will give the proper background for interpreting ocean radiances from space. In light of these needs, filtered and contrast stretched images have the advantages of physical interpretability in terms of both the radiances and their spatial distribution, and are recommended for use in the ocean and coastal zone.

SUMMARY AND CONCLUSIONS

The spectral properties of the oceanic front associated with the Loop Current have been studied by ship and satellite observations and by radiative transfer theory. It is seen that computer enhancement is required to extract useful information from the ERTS data for the ocean scene. The current boundary can be detected by changes in the surface reflectance, N_{ss}, as well as the diffuse reflectance, N_d, from below the surface; N_d however is dependent on both B and ω_0, and thus the spectral interpretation of ocean color requires surface truth measurements for meaningful results. Particle concentrations, which can delineate currents,

can be estimated in MSS 5 if the ratio $\nabla_H N_4 / \nabla_H N_5$ is reasonably constant over a scene. MSS 4 is strongly influenced by yellow substance, and particle estimation based on these data are invalid in many coastal zones. Water mass identification using ratios or differences of MSS 4, 5, and 6 data have no validity in either theory or observation in the Gulf of Mexico. Finally, it must be emphasized that the spectrum of upwelling radiance just above the surface is a function of both N_d and N_{ss} and that N_{ss} frequently dominates.

ACKNOWLEDGMENT

REFERENCES

Arvesen, J. C. (1972). Fourth Annual Earth Resources Review, Vol. IV, NASA MSC-05937, pp. 104-1 to 104-2.

Chandrasekhar, S. (1960). Radiative Transfer, Dover, New York, 393 pgs.

Charnell, R. L. and G. A. Maul (1973). Nature, Vol. 242 (5398), pp 451-452.

Cox, C. and W. Munk (1954). J. Opt. Soc. Am., 44(11), pp. 838-850.

Duntley, S. Q. (1972). Fourth Annual Earth Resources Review, Vol. IV, NASA MSC-05937, pp. 102-1 to 102-25.

Ednoff, M. (1974). Master's Thesis, Florida State University, Department of Oceanography, Tallahassee, Florida.

Galtsoff, P. S. (ed.). (1954). Gulf of Mexico - it's origin, waters and marine life. Fish and Wildlife Service, Fishery Bulletin 89, 604 pp.

Gordon, H. R. (1973). Appl. Opt., 12, pp. 2804-2805.

Gordon, H. R. and O. B. Brown (1973). Appl. Opt., 12, pp. 1549-1551.

Gordon, H. R. (1974). To be published in J. Opt. Soc. Am.

Hansen, D. V. and G. A. Maul (1970). Remote Sensing of Environment, 2, pp. 161-164.

Jerlov, N. G. (1968). Optical Oceanography, Elsevier, New York, pg. 56.

Klemas, V., J. F. Borchardt, and W. M. Treasure (1973). Remote Sensing of Environment, 2(4), pp. 205-221.

Leipper, D. F. (1970). J. G. R. 75(3):637-657.

Lorenzen, C. J. (1966). Deep Sea Research, 13, pp. 223-227.

Maul, G. A., (1972). Interim Report on Remote Sensing of Ocean Currents from ERTS, NASA-CR-12907, National Technical Information Center, E72-10233.

Maul, G. A. (1973). Symposium on Significant Results Obtained from the Earth Resources Technology Satellite-1. NASA SP-327, Vol. I (B), pp. 1365-1375.

Maul, G. A. (1974a). Transactions, A.G.U., 55(4): 283.

Maul, G. A. (1974b). Proceedings of Marine Environmental Implications of Offshore Drilling in the Eastern Gulf of Mexico, S.U.S.I.O., St. Petersburg, Florida. pp. 87-96.

Maul, G. A. and D. V. Hansen (1972). Remote Sensing of Environment, 2, pp. 109-116.

Maul, G. A. and H. R. Gordon (1974). Third Symposium on Significant Results from ERTS (in press).

Maul, G. A., R. L. Charnell and R. H. Qualset (1974). Remote Sensing of Environment (in press).

Molinari, R. L. and J. D. Cochrane (1972). In: Contributions on the physical oceanography of the Gulf of Mexico. Gulf, Houston, pp. 149-155.

Mueller, J. L. (1973). PhD. Dissertation Oregon State University, Corvalis, Oregon, 239 numbered leaves.

Murphy, E., K. Steidinger, B. Roberts, J. Williams, and J. Jolley (1974). Limnology and Oceanography (in press).

Niiler, P. P. and W. S. Richardson, Jr. (1973). J. M. R. 31(3):144-167.

Petzold, T. J. (1972). Volume Scattering Functions for Selected Ocean Waters, Scripps Institution of Oceanography, Visibility Laboratory SIO Ref. 72-28, 82 pgs.

Preisendorfor, R. W. (1965). Radiative Transfer on Discrete Spaces, Permagon, New York, 462 pgs.

Ross, D. B. and V. Cardone (1972). Fourth Annual Earth Resources Review, Vol. IV, NASA MSC-05937, pp. 85-1 to 85-20.

Strickland, J. D. H., and T. R. Parsons (1968). A Practical Handbook of Seawater Analysis. Fisheries Research Board of Canada, Ottawa, 311 pgs.

Strong, A. E. (1973). ERTS-1 Anomolous Dark Patches, National Technical Information Service: NASA-CR-133115; E73-10747, Springfield, Va.

Tyler, J. E. and R. C. Smith (1970). Measurements of Spectral Irradiance Underwater, Gordon and Breach, New York, 103 pgs.

Tyler, J. E., R. C. Smith, and W. H. Wilson, Jr. (1972). J. Opt. Soc. Am., 62(1), pp. 83-91.

APPENDIX

In this section several ERTS-1 images of the Gulf Stream System are summarized. Each of the selected images used in this report are located in figure A.1. Frame numbers 1, 2, 3, and 5 were discussed in the body of the text and will not be repeated here. The selected images are from the area of concern as stated in the contract and does not mean that these were the only good images of the current. About 10% of the images received, that passed the 60% cloud cut-off criterion, actually had ocean current information. The rest were either in the wrong area or the current was not visible; the latter cause accounted for about 25% of the null information.

Figure A.2 was used by Maul and Gordon (1974) to study the capability of ERTS to determine the particle concentration. In that study, they showed that if

$$\frac{\nabla MSS\ 4}{\nabla MSS\ 5} = constant \qquad\qquad A.1$$

then

$$\nabla MSS\ 4\ or\ 5 \sim\ \nabla b_p/b_w \qquad\qquad A.2$$

which is in turn proportional to the gradient of the particle concentration. Along the scanline shown in figure A.2, the gradient in MSS 4 and MSS 5 has been computed using several filters; the correlation coefficient (r) has been computed for each filter pair as well. The results of using different low pass filters and filter lengths are summarized in figure A.3.

The general trend is that r increases with longer filter kernels and with lower pass filters. This means that the gradient on the earth's surface with 8 km (100 sample low pass) spatial scale, has greater coherence between bands. It is not certain as to why the small scale correlation coefficient is so low. This area has significant amounts of coastal sediments which are rich in organics, and thus the Gelbstoff concentrations probably vary over a wide range.

In the images to follow, the interpretations given are based on the discussion in the text. Only one band is given in the appendix, but all were studied for interpretation. Clouds were identified in MSS 6 and MSS 7 and were optically masked out of the image before study, so that the data discussed are water phenomenon and not an atmospheric contribution. Water color shift from green to blue was made by studing if the variation in MSS 4 disappeared in MSS 5; if so, the color of low radiance scanspots in MSS 4 must be bluer than the higher radiance data. Similarly sediments are not seen in MSS 7 or frequently even in MSS 6; clouds are always seen in all four channels. The images are presented for the general use of other marine scientists without discussion except for the figure captions.
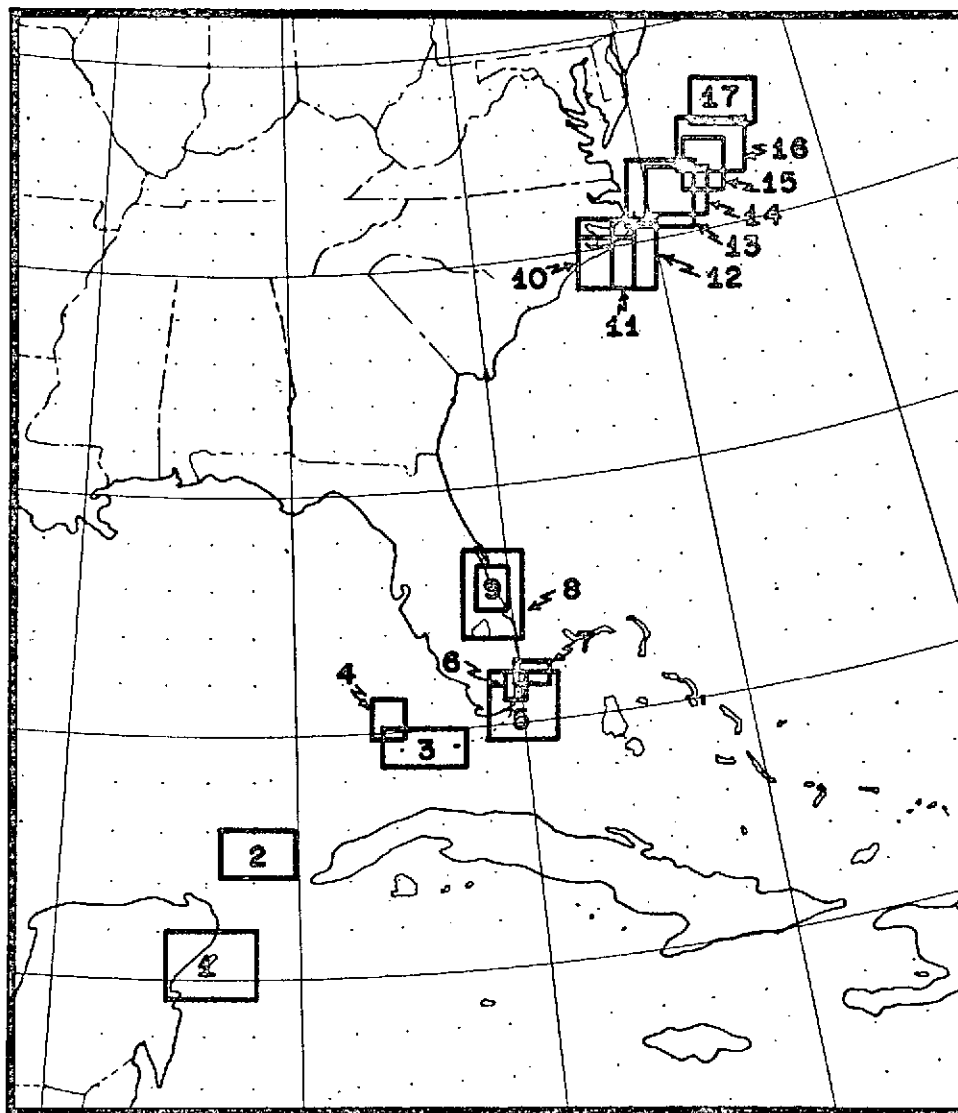
Figure A.1 Location map of selected images in appendix A. Images 1, 2,
3, and 5 were discussed in the text and are not repeated here.
Images 4, 6-17 are labeled figures A.4, A.6-A.17; there is no
A.5 and A.1-A.3 are used for introductory discussion.

S E E   F I G U R E   1 3

Figure A.2 Contrast stretched ($4 \le DN < 12$; $n=2$) negative MSS 5 image of
the ocean area offshore of Cape Hatteras (ERTS ID 1132-15042)
observed on 2 December 1972. The Gulf Stream can be seen as
the bright area to the south of the entrained sediment from
the coastal estuaries. The least squares fit of eq. (17) was
done along the scanline north of the Cape and extending from
nearshore, through the suspended sediment and into the current.
Extensions of this plume were observed for 150 kilometers
further east on other ERTS images. Horizontal distance across
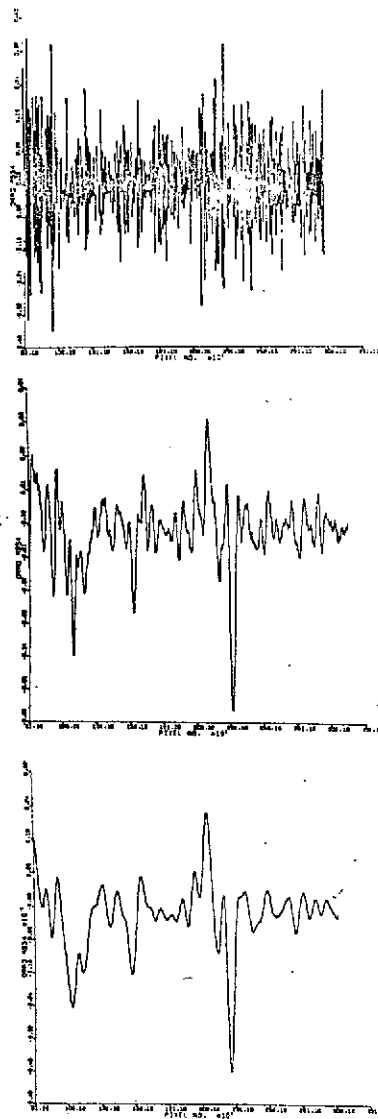the image is 135 kilometers.

Figure A.3   Gradient of radiance received at the satellite in MSS 4 along
the ocean line shown on figure A.2.   Scan spot numbers arbe-
trarily start at 1 which is just off the image in the previous
figure and over the coast.   Correlation coefficient (r) for
the MSS 4-MSS 5 linear correlation is: upper - 10 sample low
pass (199 element kernel), r=0.085; middle - 100 sample low
pass (59 element kernel), r=0.398; lower - 100 sample low pass
(159 element kernel), r=0.698.   Compare with figure 14 for 100
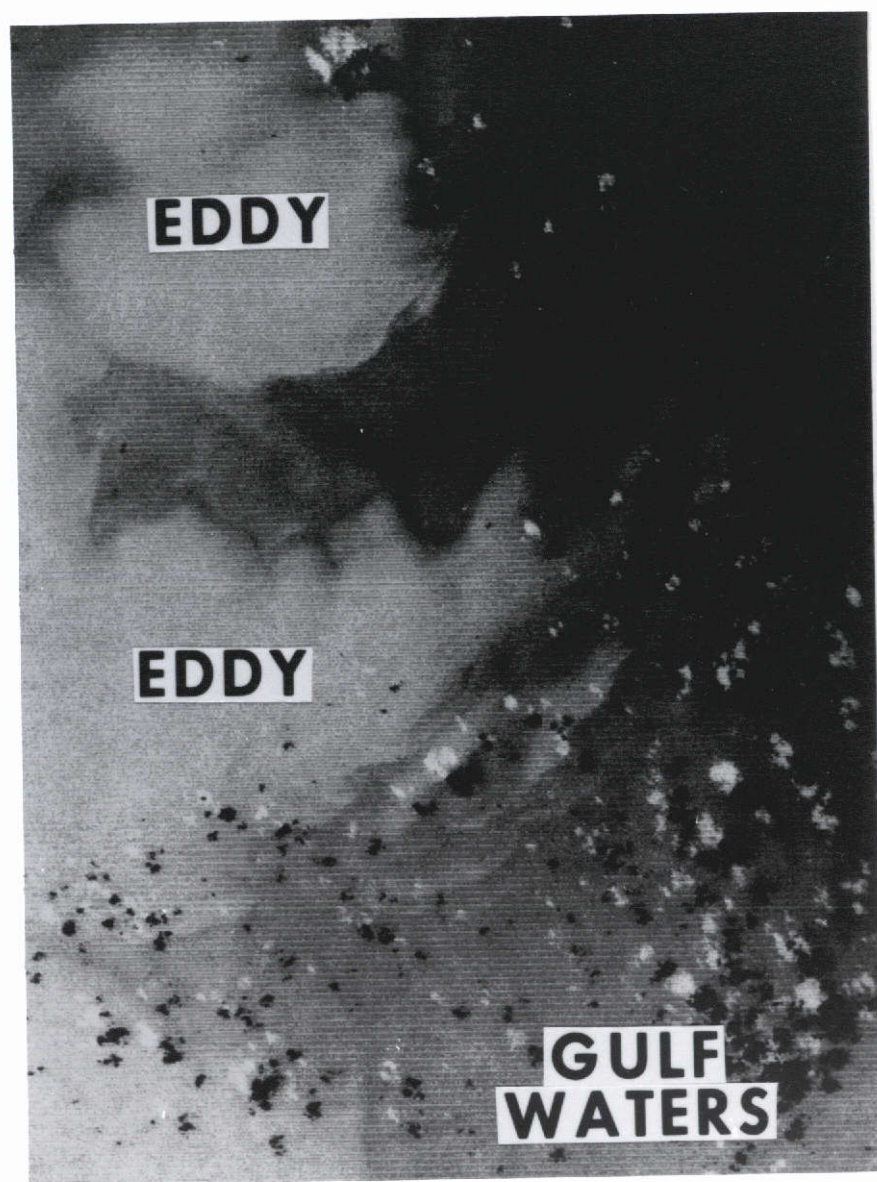sample low pass using 199 elements in the filter kernel, where
r=0.740.

Figure A.4 Contrast stretched ($16 \leq \overline{DN} \leq 24$; n=1) negative MSS 4 image of eddies in the eastern Gulf of Mexico (ERTS ID #-1153-15292) observed on 23 December 1972. The eddies were visible in only one band and therefore are minus green in color. This implies that they are spin-off eddies from the Gulf Loop Current that have come onto the west Florida Platform where they will eventually spin down exchanging momentum, nutrients, and heat with that water mass. Horizontal distance across the image is 45 km which means the eddies are 20 km. Sense of rotation is unknown but probably anticyclonic.
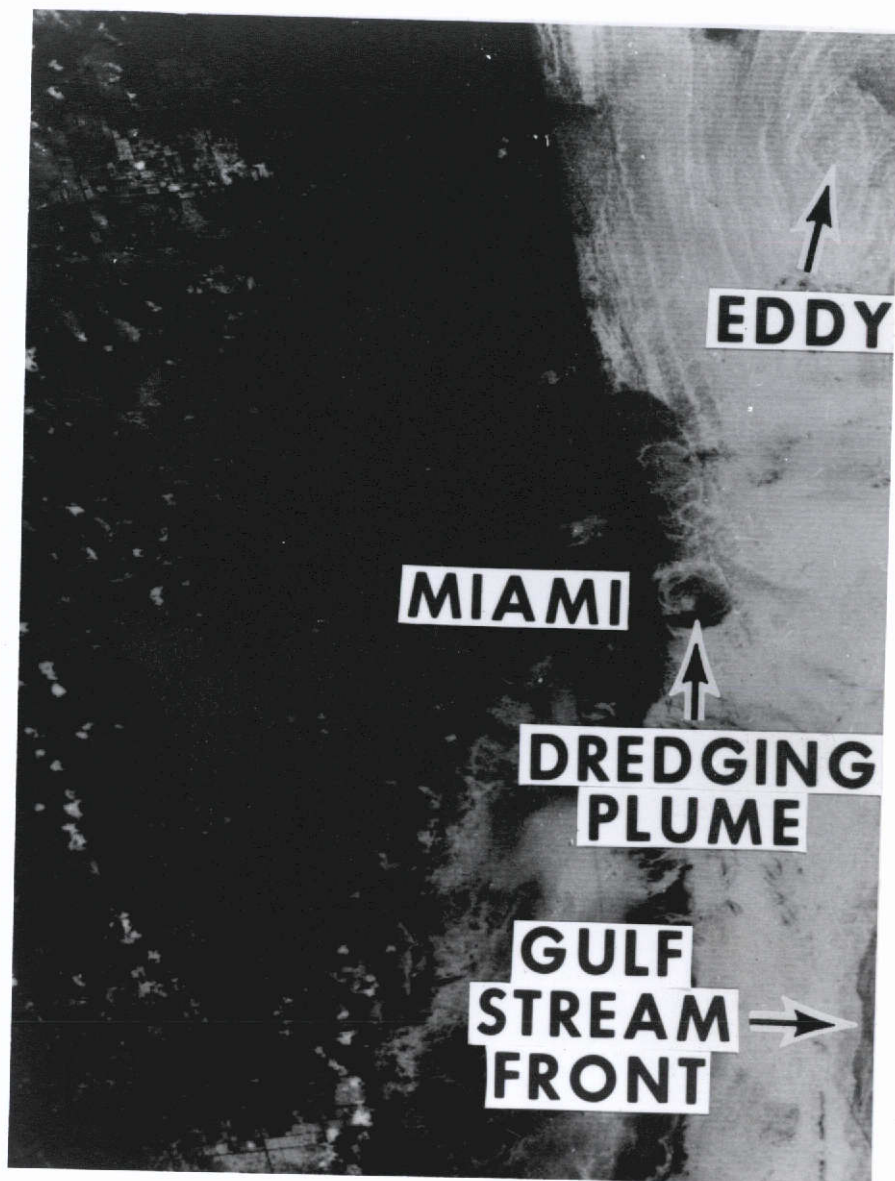
Figure A.6 Contrast stretched (12 < DN < 21; n=1) negative MSS 5 image of
Miami, Florida (ERTS ID 1350-15231) observed on 8 July 1973.
Government Cut and the Miami harbor basin were being dredged
when this image on the ebb tide was taken. The dredge spoils
can be seen as a jet flowing out into the shelf where a cyclon-
ic circulation is caused by the Longshore drift. A cyclonic
eddy, either spin-off or shear induced (Lee, 1974) by the Gulf
Stream is seen in the upper right due to changes in surface
reflectance. The Gulf Stream front at the lower right is seen
due to higher radiance in the current. Complications of near-
shore currents can be deduced because the offshore eddy and
the northern inlets have a southward inshore drift that has
reversed or slackened near the dredging plume. Horizontal
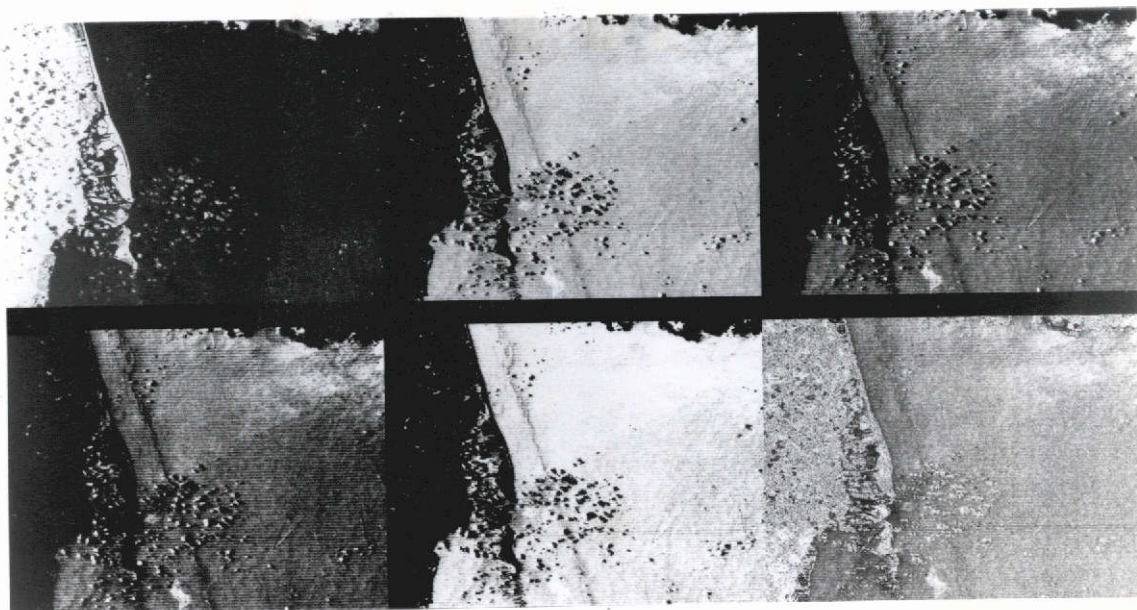distance across the image is 45 km.

Figure A.7 Contrast stretched sequence of MSS 6 data off Miami Beach, Florida (ERTS ID-1026-15230) observed on 18 August 1972. Sequence shows the effect of varying the DN range and n in the contrast equation. a) Upper left: Raw data, positive print. b) Upper middle: $7 < DN < 15$; $n=1$. c) Upper right: $7 < DN < 15$; $n=3$. d) Lower left: $7 < DN < 11$; $n=1$. e) Lower middle: $9 < DN < 13$. f) Lower right: MSS 6 minus MSS 7 then $5 < DN < 13$; $n=3$. Note that using powers of n brings out water details (cf. b & c) as does lowering the upper limit on DN (cf. b & d). Water details in e are less distinct than in b which uses the statistically determined limits. Sea state only is observable in MSS 7 so MSS 6-MSS 7 should minimize the surface contribution as is shown in f. Horizontal distance across each image is 45 km.
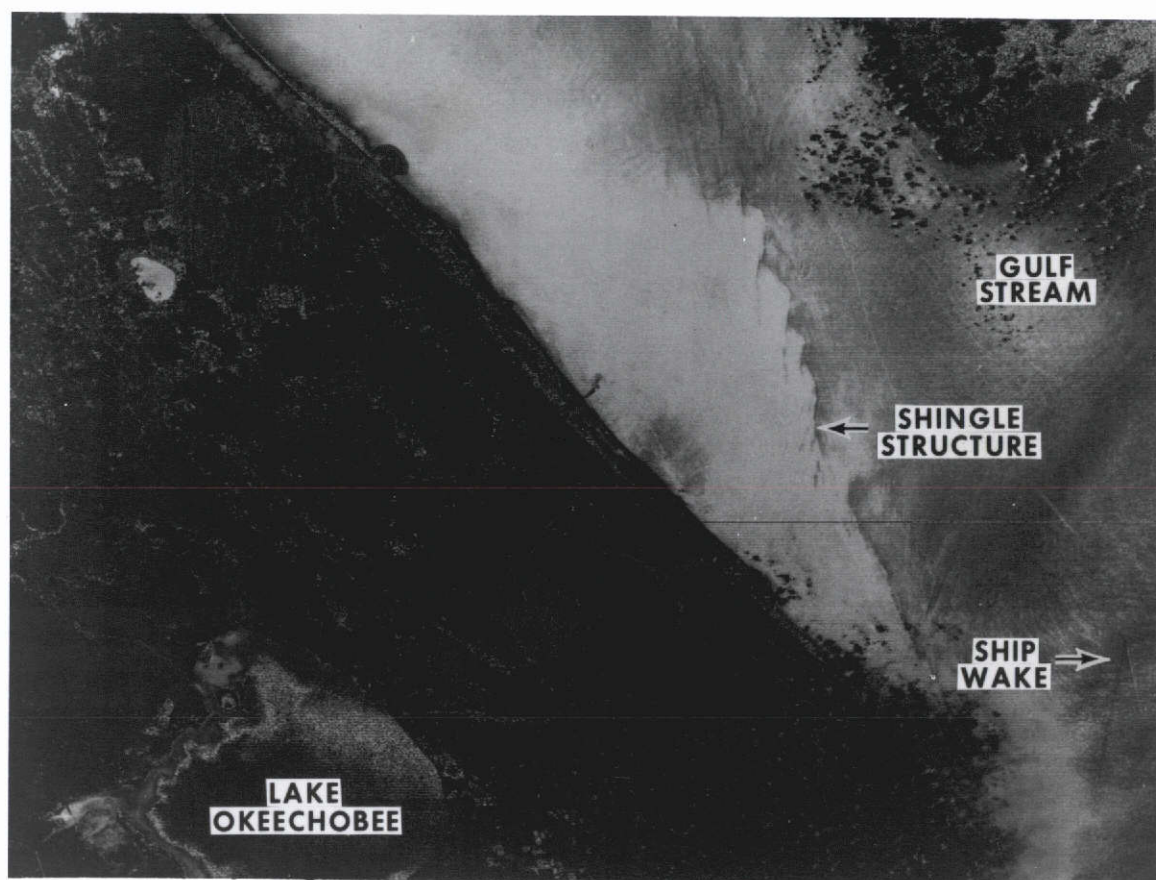
Figure A.8 Contrast stretched ($9 \leq$ DN ≤ 17; n=1) negative MSS 5 image of the region offshore of Cape Canaveral, Florida (ERTS ID 1260-15233) observed on 9 April 1973. Fine scale "shingle structure" (von Arx, Bumpus, and Richardson, 1955) can be seen along the cyclonic edge of the Gulf Stream. The shingle structure in this image is at least an order of magnitude less than von Arx et al. description off the Carolinas. Wind streaks and a ship wake can be observed in the Gulf Stream which is leaving the coast at the lower right. Loss of water detail in Lake Okeechobee is caused by the contrast stretch limits and shows that the very high radiance from this water body is due to a turbidity about equal to the coastal inlet plume in the upper left. Horizontal distance across the image is 135 km.
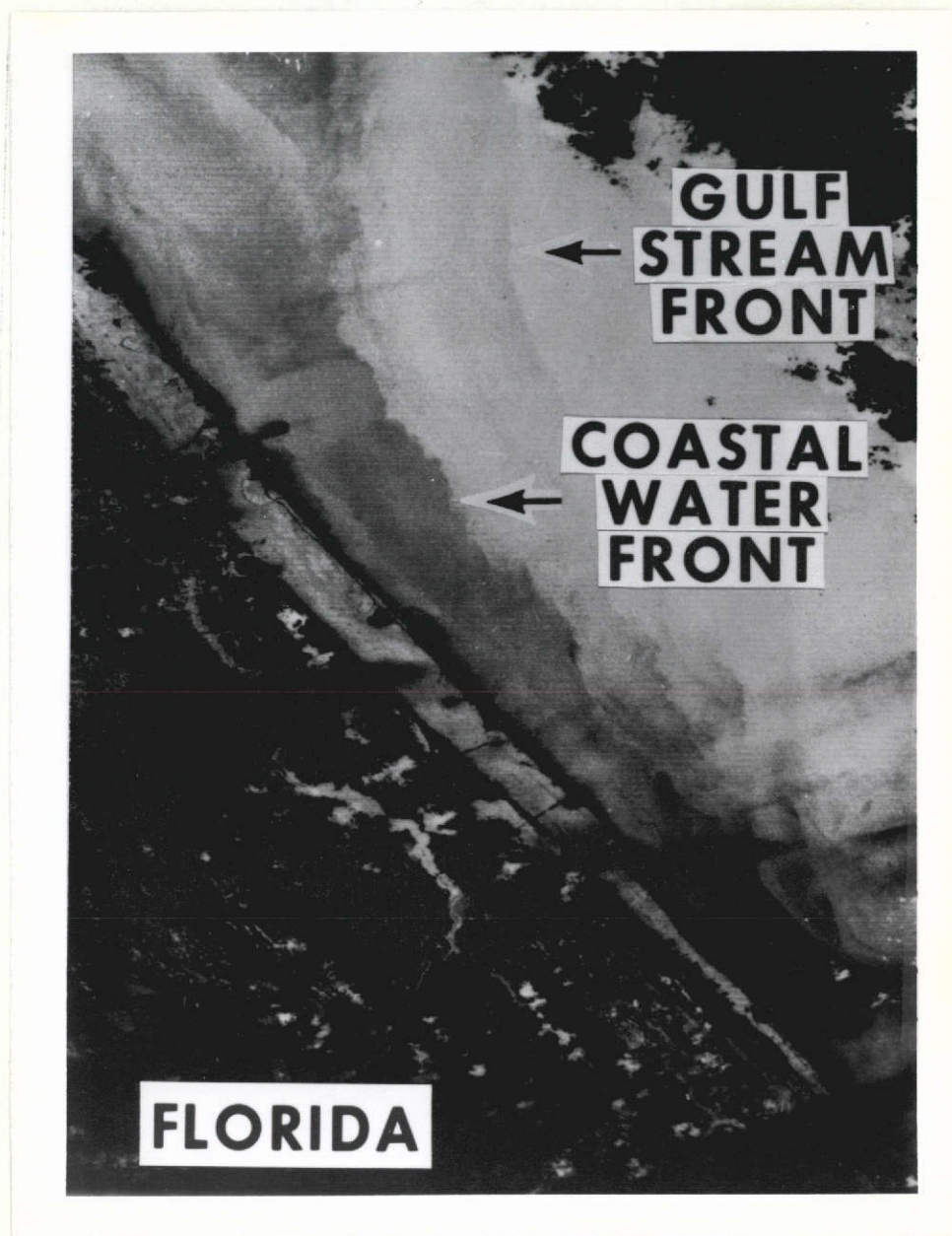
Figure A.9 Contrast stretched (8 < DN < 16; n=1) negative MSS 5 image of
the Florida coast south of Cape Canaveral (ERTS ID 1206-15232)
observed on 18 August 1972. Plumes of water from behind the
barrier islands can be seen ebbing through the inlets. Com-
plicated patterns of coastal sedimentation show a multifronted
boundary between the nearshore water and the Gulf Stream.
Changes in the radiance appear to be dominated by changes in
suspended sediments. Horizontal distance across the image is
45 km.

Figure A.10   Contrast stretched (7 $\leq$ DN $\leq$ 15; n=2) negative MSS 5 image of
Cape Lookout, North Carolina, (ERTS ID-1115-15152) observed
on 14 November 1972. The shoals offshore of the promitory
are shallow and keep sediments in suspension. By comparing
the sediment pattern over such areas (cf. A.11) an estimate
of the bottom topography can be made, and conversely, the
variability of the suspended load as well. There is no
evidence of the Gulf Stream front in this image. Horizontal
distance across the image is 135 km.

Figure A.11 Contrast stretched (4 < DN < 11; n=1) negative MSS 5 image of Onslow Bay, North Carolina (ERTS ID-1205-15153) observed on 13 February 1973. Complex patterns of turbidity do not appear to be well correlated with the bottom topography. The white pixels near the coast are an artifact of the contrast stretch routine wherein the NOAA computer assigns a negative zero to the upper cutoff value (DN=11 in this case). When the negative zero is reformatted onto the digital-to-analog tape, it inadvertently becomes a maximum value which appears on the image as a white pixel. The scene appears gray because black (DN>11) and white (DN=11) values are intermixed. This does not appear in images with n≥2, and has been corrected for. Horizontal scale distance across the image is 135 km.
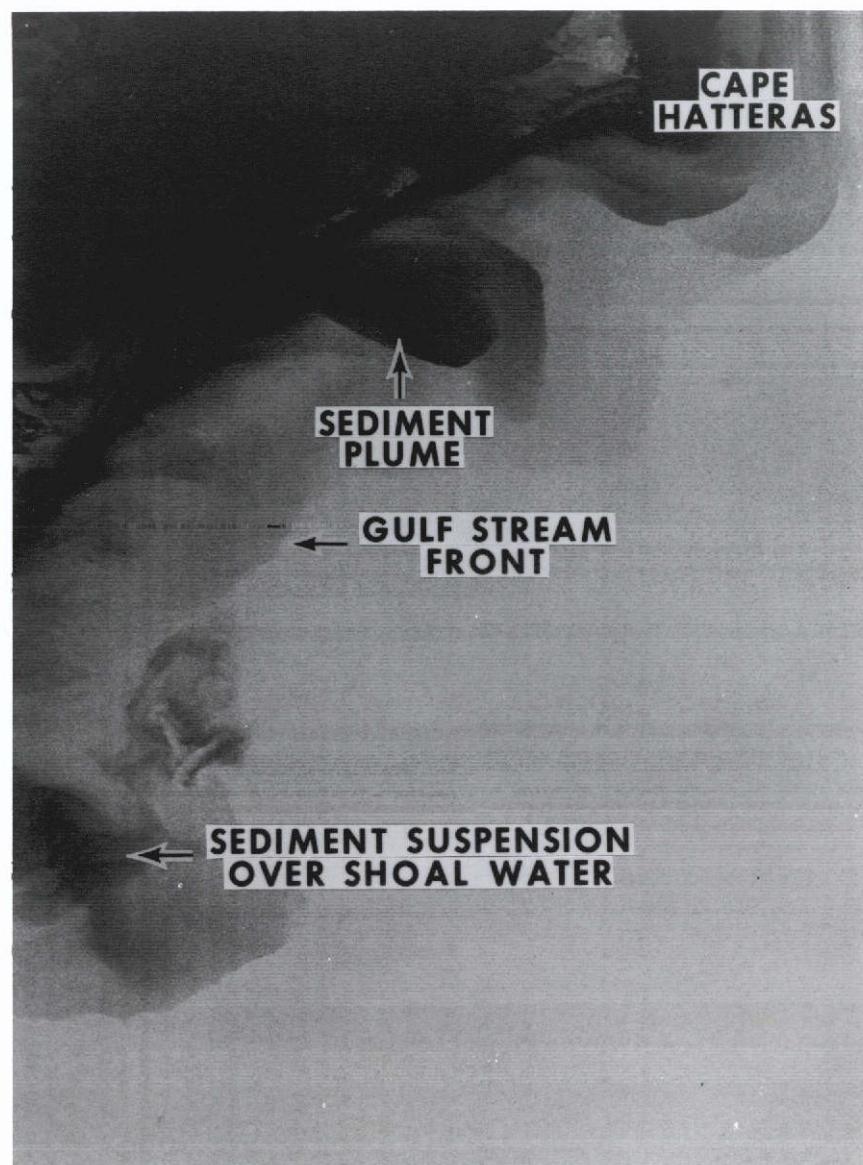
Figure A.12 Contrast stretched (5 ≤ DN ≤ 13; n=2) negative MSS 5 image of the Cape Hatteras, North Carolina area (ERTS ID-1132-15094) observed on 1 December 1972. Mairs (1970) correlated the pulses in the Ocracoke Inlet sediment plume to several stages in the tide. The Cape Hatteras materials are transported from further north, and an eddy has been observed in several ERTS images in the Hatteras region. Compare again the sediment suspension over Lookout Shoals with the scene in figures A.10 and A.11; detail changes are due to both different stretch limits as well as environmental conditions. Horizontal distance across the image is 90 km.
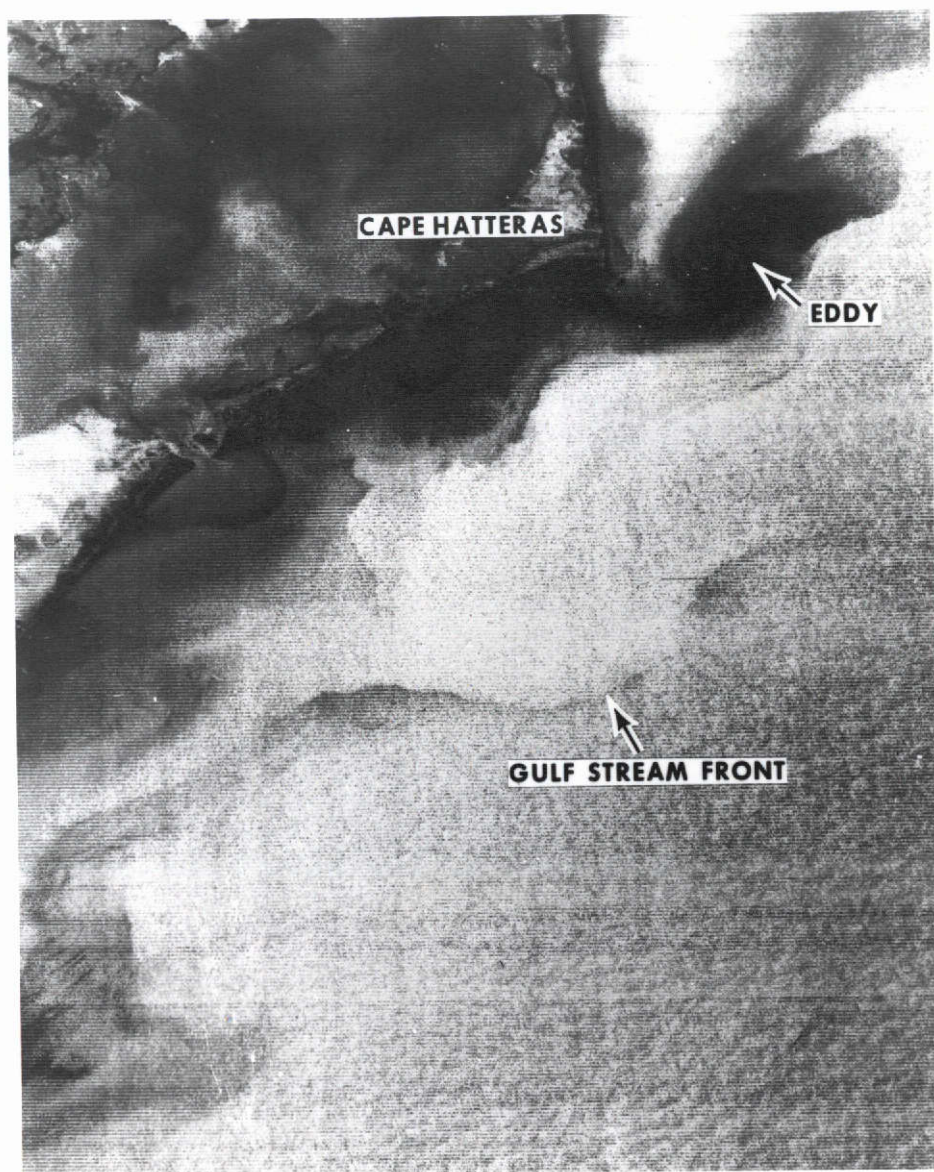
Figure A.13   Contrast stretched (14 ≤ DN ≤ 22; n=2) negative MSS 4 image of
an eddy over Diamond Shoals, North Carolina (ERTS ID 1186-
15093) observed on 25 January 1973. A deep penetration of
water from north of Cape Hatteras can be seen as part of the
cyclonic eddy developing over the shoals. The Gulf Stream
front appears to be well offshore of the eddy front. Meander
scale in the Gulf Stream appears to be about 50 km with an
amplitude of about 10 km. Details in the sediment suspension
patterns supports the notion of multiple fronts, probably
tidally pumped and advected by alongshore current patterns.
Streaks can be seen in the current at the lower right and may
be internal wave activity. Horizontal distance across the
image is 90 km.

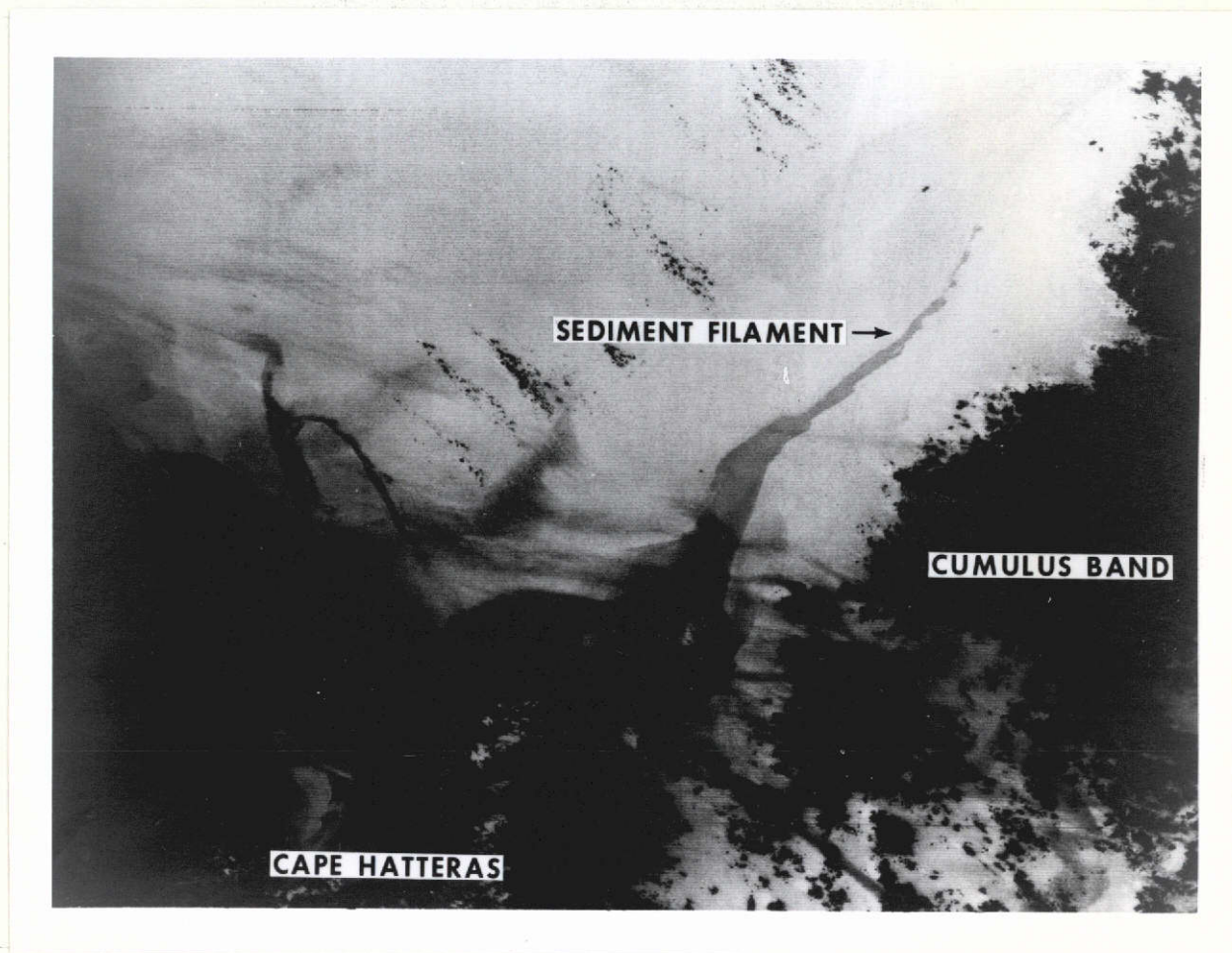Image labels: SEDIMENT FILAMENT →, CUMULUS BAND, CAPE HATTERAS

Figure A.14   Contrast stretched ($7 \leq DN \leq 15$; n=2) negative MSS 5 image of a sediment filament in the offing of Cape Hatteras, North Carolina (ERTS ID 1222-15093) observed on 2 March 1973. The squaring in the stretch equation over-accenuates the low radiance features so that details at Cape Hatteras are lost; generally n=1 is a better choice because it is linear with radiance for spectral comparison purposes. The sediment filament extends 120 km offshore and is probably material from Pamlico Sound as Ford, Longard, and Banks (1952) have suggested in their entrainment studies. Horizontal distance across the image is 135 km.
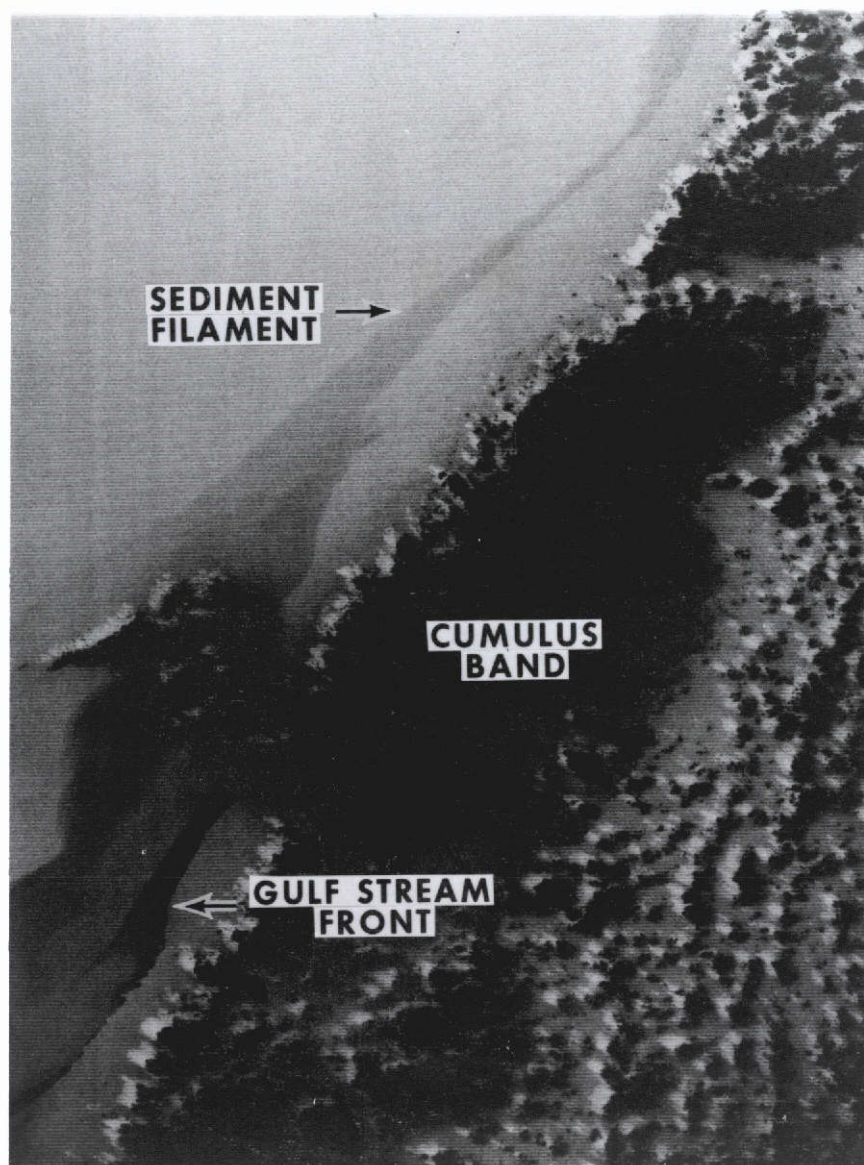
Figure A.15 Contrast stretched (16 $\leq$ DN $\leq$ 24; n=3) negative MSS 4 image of the Gulf Stream in deep water off Cape Hatteras (ERTS ID 1221-15035) observed on 1 March 1973. Taken one day earlier than A.14 this plume is over 180 km long on this image and extends over 300 km from Cape Hatteras. The cumulus band is a frequent feature of the stream from space and is caused by the convection when cool dry continental air is heated by the stream. This feature follows the Gulf Stream front quite well as seen in the image and can be used as an ancillary feature for identification of the Stream. Horizontal distance across the image is 90 km.
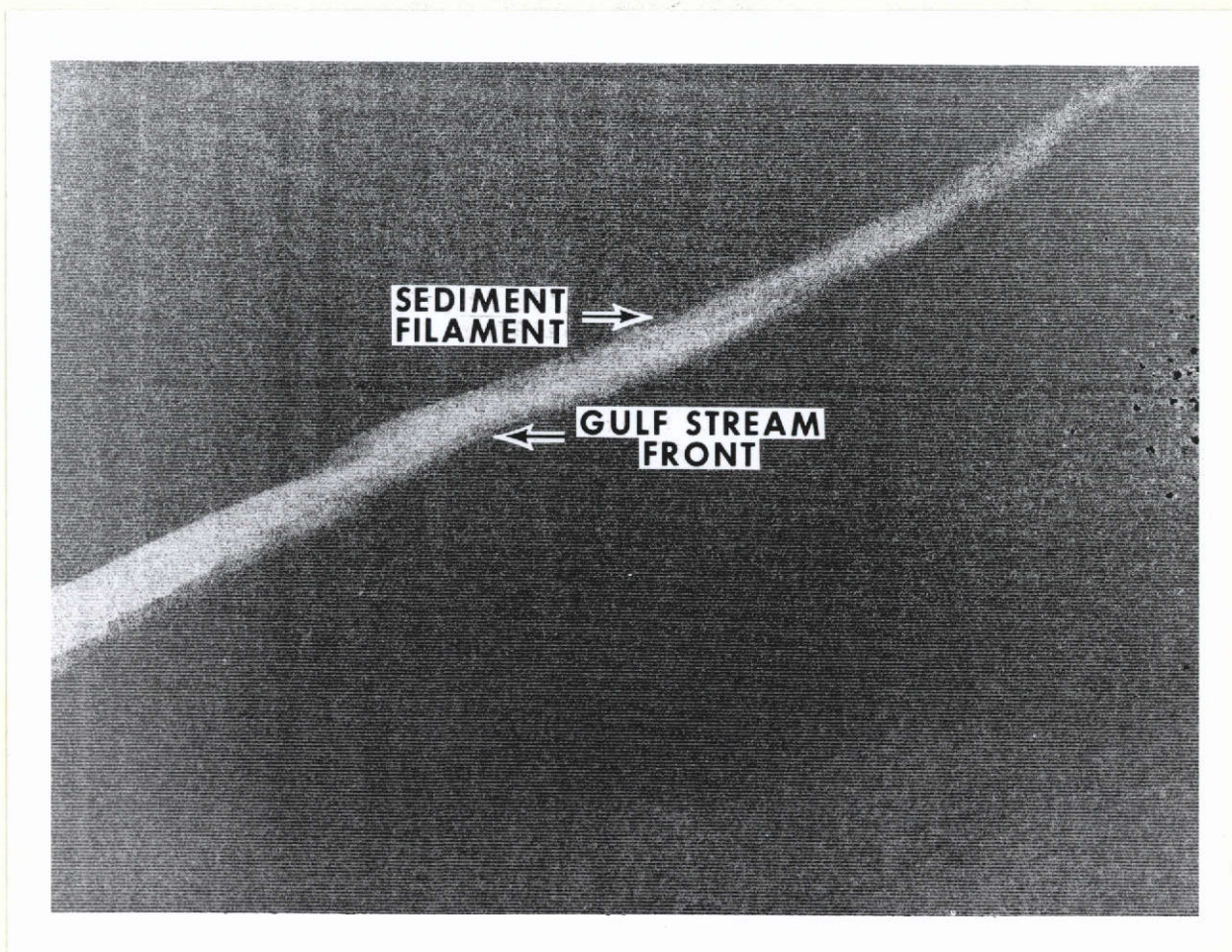
Figure A.16   Contrast stretched (12 $\leq$ DN $\leq$ 16; n=1) negative MSS 4 image of
a sediment filament offshore of Cape Hatteras, North Carolina
(ERTS ID 1149-15033) observed on 19 December 1972. This
image was observed 17 days later than the data in A.2, but is
an almost perfect extension of that sediment filament and ex-
tends about 270 km to sea. Note the DN limits have a range
of only 5. The Gulf Stream waters are at the same intensity
as the waters on the north of the sediment filament and the
Stream is observable only because little small scale mixing
has occurred across the boundary. Horizontal distance across
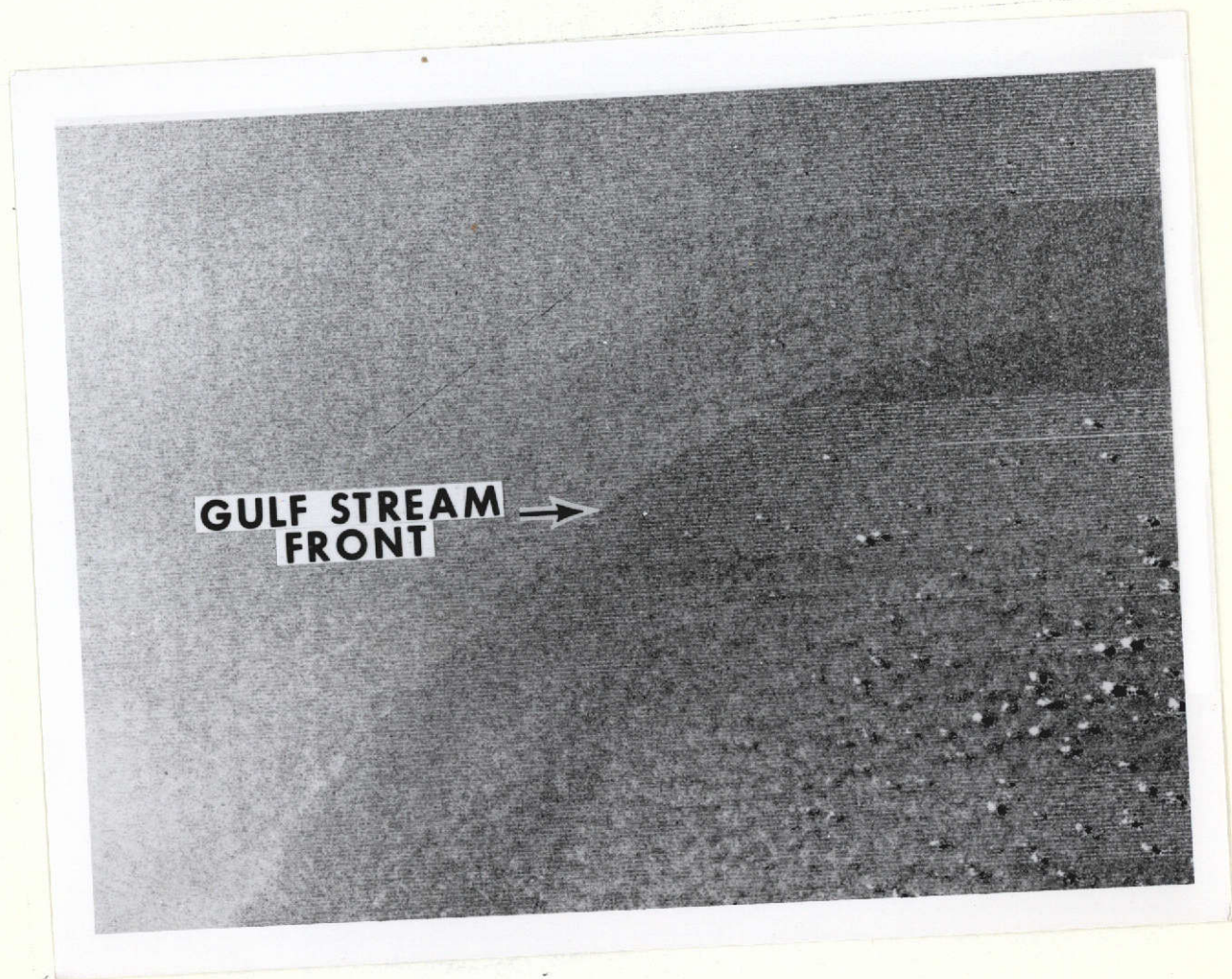the image is 135 km.

Figure A.17 Contrast stretched (11 $\leq$ DN $\leq$ 15; n=1) negative MSS 5 image of the Gulf Stream off Delaware (ERTS ID 1257-15033) observed on 6 April 1973. The stream is observable in this case due to higher radiance caused by increased sea state in the flow. This image is 350 km northeast of Cape Hatteras. There is a hazard in using sea state only to identify the current because even in MSS 7 a slight increase in radiance occurs which could be caused by high thin cirrus clouds. Horizontal distance across the image is 135 km.